Chapter 6 Microstructure Evolution and Process Control

6.1 Introduction

A CVD process is very complex, many ignore chemical reactions and involves. To this day, it is still very difficult or impossible to identify the reactant species and reaction paths during a CVD process at high temperature by experimental methods. Meanwhile, various physical and chemical phenomena are involved in the deposition process. For a CVD process, these phenomena include [1]: (1) heat transfer from the heating element to the substrate to activate the chemical reactions, (2) mass transport in the bulk gas and boundary layer, (3) adsorption and migration of the reactant gaseous species on the surface of the substrate, as well as the desorption of the by-product gaseous species, and (4) solid product formation from the homogeneous and heterogeneous chemical reactions. Furthermore, the situation becomes much more complex because these phenomena are always interacting with each other.

For each phenomenon, there are also many elements involved which determine the behaviour of each phenomenon. These phenomena are described by a wide range of characteristic time and length values. For the case of CVI fabrication of fibre-reinforced ceramic-matrix composites, the diameter of a molecule and the thickness of the interfacial phase are about 10^{-1} nm and 10^{2} nm respectively, whilst the sizes of the substrate/component and the reaction are around 1 m. In addition, elementary chemical reactions occur in a time range of 10^{-5} to 10^{-4} s, the time for heat transfer and mass transfer is around 1 s to 10 min. By contrast, the total densification time for one CVI run is as long as approximately 10^{2} h. In such cases, it is necessary to establish multiscale models to understand and optimise a CVD process.

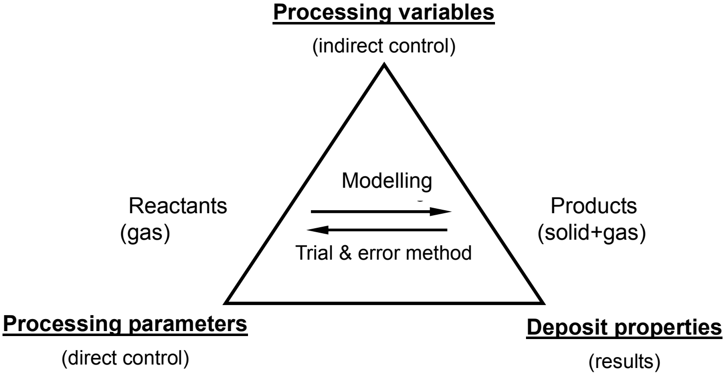

Figure 6.1. Relationships among the processing parameters, variables and properties of the deposit [2]

Table 6.1. CVD parameters, variables and properties [2]

Processing parameters (direct)	**Processing variables (indirect)**	**Deposit properties (results)**
Temperature	Temperature field	Microstructure
Flow rate	Velocity field	Characteristics
Pressure	Concentration field	Chemical composition
Deposition time	Supersaturation	Thickness uniformity
Nature of precursor	Sticking coefficient	Crystalline nature
Reaction geometry	A/V ratio	Deposition defects
Substrate/preform geometry	Residence time	Residual stress
Orientation of Substrate/preform	Coefficient of drag	Density distribution
		Growth rate

For any CVD process, the two key issues to be addressed are increasing the deposition rate and improving the quality of the matrix deposit. In order to obtain materials with desirable properties, it is necessary to strictly control the processing parameters. A phenomenological approach is usually used to establish the relationships among processing parameters, processing variables and properties of the deposit. A framework was proposed by Spear [2], as shown in Figure 6.1.

As listed in Table 6.1, some parameters such as temperature, pressure, flow rate, etc. are considered processing parameters because they can be directly used to control a CVD process and to determine the microstructure and properties of the deposit. The processing variables include temperature field, velocity field and so forth, which are the results of the system response. These are known as indirectly controlling parameters which are very important for understanding the deposition mechanism.

This chapter describes the theory of the microstructure evolution of the deposits and some control methods of a CVD process and the relationship between microstructures and processing parameters.

6.2 Microstructure Evolution of Chemical Vapour Deposition Deposits

6.2.1 Film Formation and Structure Zone Model

Thin-film formation is described as a sequential process which includes nucleation, coalescence and subsequent thickness growth, whereby all states can be influenced by deposition parameters, such as temperature, pressure, gas flow rate, etc. [3, 4]. For physical vapour deposition (PVD) processes, significant works have been published and progess made in understanding the microstructure evolution of the films. In the atomistics of growth processes, there exists much in common bewteen CVD and PVD. Theories from PVD processes can thus be used to analyse the microstructure evolution of CVD processes [5, 6].

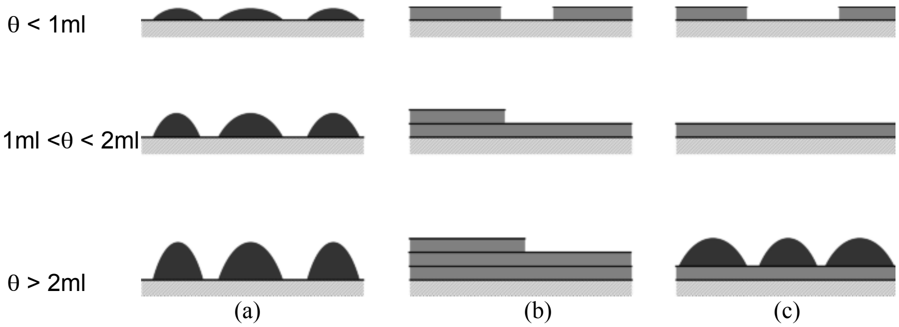

Figure 6.2. Three types of growth mode (*θ*: coverage, ml: monolayer): (a) 3-D island mode, (b) 2-D layer mode and (c) island-layer mode

At the initial stage of film deposition, a sufficient number of gaseous species are condensed to establish a permanent residence on the surface of the substrate. The model of film formation can be categorised into three basic types, which are illustrated schematically in Figure 6.2. This work was first realised by Bauer [7] and the details of these categorisations are described as follows.

6.2.1.1 Three-dimensional Island Mode (Volmer–Weber Mode)

This occurs when stable clusters small, form on the substrate surface and grow in three dimensions to form separate islands. This happens when the bonding between atoms in the clusters is much greater and stronger than that between the atom and the substrate. Many systems of metals on the insulators of micro-electronic devices display this mode of growth, such as silicon growth an SiO_2 substrate reported by Bloem [8].

6.2.1.2 Layer-by-layer Mode (Frank–Van Der Merwe Mode)

This is a kind of two-dimensional growth mode, and layers of the deposit grow on the surface of another layer. In this case, the atomic bonding between the substrate surface and the film is greater than that between atoms of adjacent film layers. The homoepitaxial growth of Si thin film Si substrate belongs to this mode.

6.2.1.3 Layer Plus Island Mode (Stanski–Krastanov Mode)

This is an intermediate combination of the two growth modes mentioned above. The substrate is first covered with one or a few monolayers grown in Frank–van der Merwe mode, then some three-dimensional islands are formed on the surface in the Volmer–Weber growth mode. This mode is a transition from two-dimensional growth to three-dimensional growth and has been observed in metal–metal and metal–semiconductor systems.

In order to characterise the morphology of deposit, several models have been proposed; the structure zone model (SZM model) was first proposed by Movchan and Demchishin in 1969 [9]. Based on the observation of the microstructure characteristics of Ti, Ni, W, ZrO_2 and Al_2O_3 coatings by electron beam evaporation, they established the structure zone model in terms of three zones, which was used to describe the relationship between the morphology and the processing

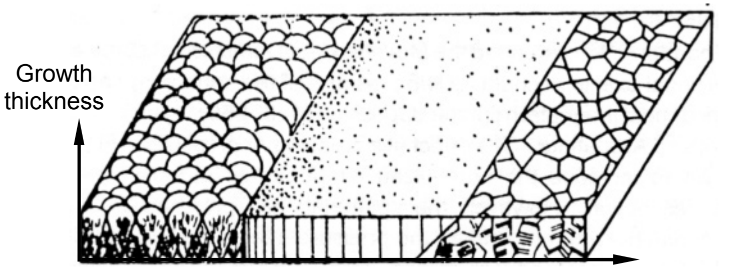

(a)

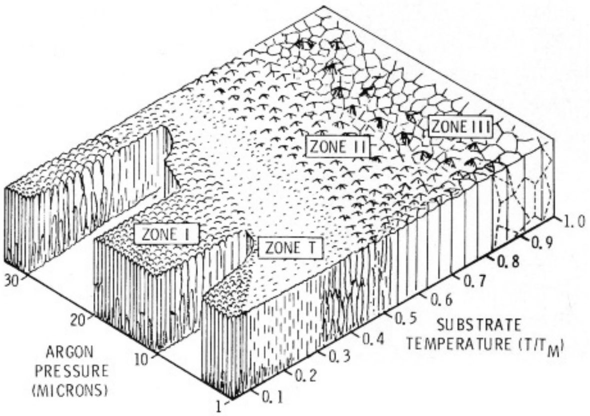

(b)

Figure 6.3. Structure zone model: (a) Movchan and Demchishin model [9] and (b) Thornton model [11]

temperature parameter (T/T_m). Here, T is the substrate temperature and T_m is the coating-material melting point. Later, Thornton [10, 11] introduced a second parameter of sputtering gas pressure and a transition zone (T_{trans}) between zones I and II. As shown in Figure 6.3, each zone has its own distinct characteristic structures and deposit properties.

(i) Zone I ($T/T_m < 0.3$)

This zone is characterised by a lower T/T_m ratio and consists of tapered crystals with domed tops which are separated and have voided boundaries. The internal structure of the crystals is poorly constructed and the crystal defect (e.g. dislocation) density is very high. The size of the crystallite increases with an increase in the T/T_m ratio. This dependence implies that there is very little surface diffusion. Accordingly, the metals fabricated by PVD techniques exhibit great hardness but weak lateral strength. This zone is associated with coating-flux shadowing that is not overcome by atom surface diffusion.

(ii) Zone T_{trans} (conical columnar structure)

The T_{trans} zone is a transitional zone between zones I and II. The coating in this zone consists of dense arrays of poorly defined fibrous grains without a voided boundary. At relatively high temperatures, surface diffusion becomes very evident; however, grain boundary diffusion is strongly limited. Grain coarsening occurs during coalescence of the small islands which have a high surface-area-to-volume ratio. During the coarsening process, the orientation of the crystal is determined by the T/T_m ratio; thus crystallites are nearly random or only weakly textured. In this case, there is a wide distribution of grain sizes.

(iii) Zone II ($0.3 < T/T_m < 0.5$)

The coating grown in this zone at higher substrate temperatures consists of columnar grains separated by distinct, dense and intercrystalline boundaries. The deposit has a smooth surface. The size of the grain is further increased with an increase in the T/T_m ratio and may extend through the coating thickness if the processing temperature is sufficiently high. If it is, the mechanical properties of the metallic deposits by the PVD processes are comparable to those of the cast metals.

This zone is characterised by high substrate temperatures at which both surface and grain boundary diffusion occur at significant levels. A homogeneous structure is obtained through the film thickness and is composed of columnar grains from the bottom to the top of the film. The grain boundaries are nearly perpendicular to the surface of the substrate.

(iv) Zone III ($0.5 < T/T_m < 1$)

This one consists of equiaxed grains with a high density, resulting in a bright surface. The surface diffusion, grain boundary diffusion and bulk diffusion are all operative. Therefore, secondary recrystallization of the deposits occurs and the degree of texture is considerably enhanced. The equiaxed grains obtained imply that the crystal growth of the deposits is regularly blocked.

Active energies for surface, grain boundary and bulk diffusion are typically in the ratio of 1:2:4. Here, surface diffusion occurs with active energy in the range 0.1 to 0.3 eV, and the bulk diffusion occurs with activation energies above 0.3 eV [3]. During island coalescence, there is a strong driving force for coarsening through surface atom diffusion and grain boundary (GB) movement, which is due to the free energy decrease as discussed by the classical theory of crystal growth. The islands with lower free energy atoms consume the islands with high free energy, resulting in a new larger island as the system attempts to minimise the overall surface energy.

6.2.2 Microstructure Characteristics of Chemical Vapour Deposition Deposits

6.2.2.1 Influence of Supersaturation and Temperature on Deposit Microstructure

For a CVD process, the depositing parameters affect the nucleation and growth modes which in turn influence the microstructure and properties of the deposited material. The driving force of the nucleation is the supersaturation in the CVD reaction system. The supersaturation in the gaseous reactions can be analogous to the supercooling in the solidification process for metal materials. For a general chemical reaction,

$$aA_{(V)} + bB_{(V)} = cC_{(S)} + dD_{(V)} \tag{6.1}$$

Supersaturation is defined as the ratio of the product of the gas-phase partial pressures in the real state to the product of the corresponding equilibrium partial pressures and is expressed by [12]

$$\gamma = \frac{p_A^a p_B^b p_D^d}{p_{Ae}^a p_{Be}^b p_{De}^d} \tag{6.2}$$

where p_A, p_B and p_D are the partial pressure of gases A, B and D in the real state respectively; p_{Ae}, p_{Be} and p_{De} are the partial pressures of gases A, B and D in the equilibrium state respectively.

Accoring to the processing conditions of a CVD process, supersaturation can be divided into two categories, bulk supersaturation and local supersaturation [13]. If a CVD process occurs in the chemical reaction control regime discussed in Section 4.3.4, it is reasonable to assume that the compositions of a gas on the substrate surface equal that in the bulk gas. Accordingly, the expression of supersaturation in Equation (6.2) is used for calculation. However, if a CVD process occurs in the

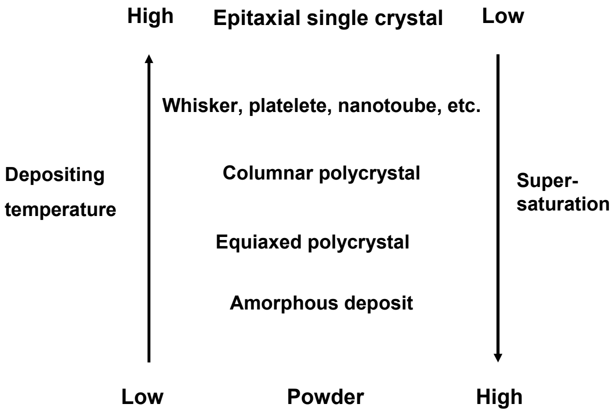

Figure 6.4. Relation of supersaturation and temperature to morphology [15]

mass transport regime, a significant concentration gradient will exist within the boundary layer near the substrate surface. In this case, the local supersaturation is difficult to calculate and it is considerably lower than that of the bulk gas.

Based on the observations of PVD, Blocher established morphological dependence on supersaturation and temperature as shown in Figure 6.4. According to Bryant's investigation [14], the same sort of dependence exists for CVD materials [15].

Epitaxial Growth

Materials with an epitaxial structure have been widely used in semiconductor and superconductor applications. Epitaxial growth occurs at a relatively high depositing temperature but with a low supersaturation. For example, the 4H–SiC epitaxial growth from SiH_4–C_3H_8 gases is conducted at 1700 to 1900°C [16], whilst the β-SiC polycrystal growth from CH_3SiCl_3–H_2 gases is fabricated at a temperature of around 1000°C. Such deposits exhibit the same orientation as the substrate material and perfect crystal structure because the atoms have sufficient activities for surface diffusion, grain diffusion and bulk diffusion. Therefore, the nucleation and growth of the deposit take place in the particles' preferred orientation, which has the minimal interfacial free energy among all orientations. The epitaxial growth of a single crystal is usually performed at reduced pressure.

Whiskers/Platelets/Nano-Belts/Nano-Tubes/Coiled Fibres

A whisker is fabricated according to the vapour-solid or vapour-liquid-solid mechanisms with the aid of certain special catalysts [17]. It involves nucleation at preferred locations such as the terrace, ledge and kink on a substrate surface, and defects in crystal structures developed along a special direction of impingement of nuclei. Two-dimensional and three-dimensional microstructures have also been

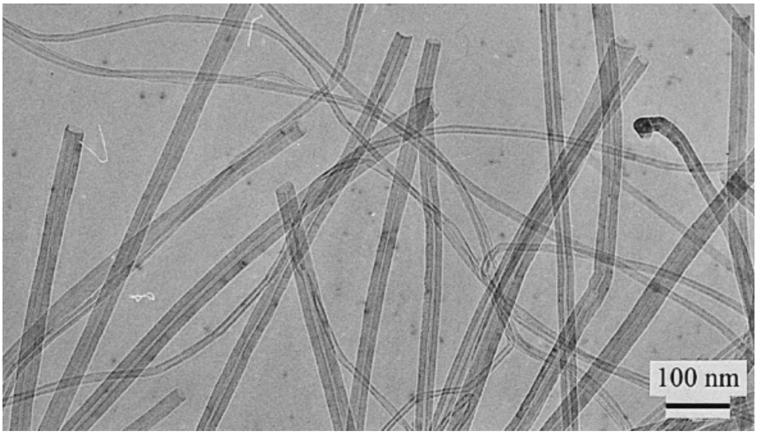

Figure 6.5. Carbon nanotubes by chemical vapour deposition [18]

successfully produced, including platelets, nanobelts, nanotubes in Figure 6.5 [18] as well as microcoiled fibres [19]. However, the formation mechanisms of these unique microstructures are very complex and further research should be carried out on these topics.

Polycrystal Growth

Both columnar and equiaxed microstructures are obtained from polycrystal growth. Columnar microstructure is composed of columnar grains of preferred orientation that grow from the first nucleated location on a substrate surface. The microstructure is attributed to high supersaturation and low temperature and hence more limited diffusion. A columnar microstructure is suitable for high-temperature structural applications, such as thermal barrier coatings. Figure 6.6 shows the typical columnar CVD SiC microstructure in C/SiC composites.

An equiaxed microstructure is comprised of small randomly oriented grains. Deposited materials with an equiaxed microstructure have superior mechanical properties according to the Hall–Petch equation [20]. They are desirable for structural applications. Such a microstructure is formed at an even higher supersaturation which ensures a sufficient amount of nuclei generated from the heterogeneous reaction on the substrate surface. The lower depositing temperature significantly limits surface diffusion and restrains the migration of atoms to preferred crystal lattice sites.

Amorphous Deposit

If the depositing temperature is sufficiently low, an amorphous deposit structure is formed because the atoms absorbed on the substrate surface are strictly constrained to the specific location, thus no further migration takes place. Two examples are amorphous silicon (a-Si:H) and silicon carbide (a-SiC:H) films with a high

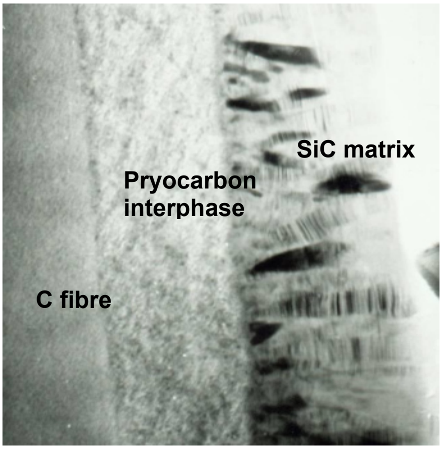

Figure 6.6. Columnar SiC in carbon-fibre-reinforced silicon carbide composites [18]

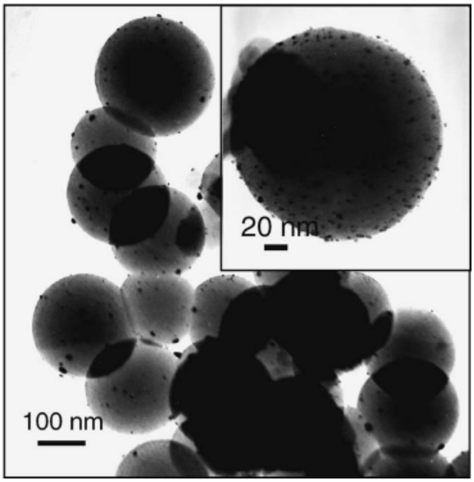

Figure 6.7. CVD Pt nanoparticles from $Pt(CH_3)_2(cod)$ deposited on C nanospheres [23]

hydrogen content [21, 22]. In order to decrease deposition temperature to approximately 300°C (less than the melting point of a polymer), it is necessary to use some enhancement methods such as plasma. Amorphous deposits have been extensively used in transistors, memory switches and solar energy conversion devices because of their wide band gap and optical energy gap.

Powder

At sufficiently high supersaturation and very low temperature, the frequency of molecular collisions within the gas phase is great enough to cause homogeneous nucleation and growth of powder-like product. Up to the present, CVD has been an important technique for manufacturing superfine powders as discussed in Section 3.7.1, or surface modification of functional powders as shown in Figure 6.7.

6.2.2.2 Microstructure of Chemical Vapour Deposition SiC

Figure 6.8 shows the X-ray diffraction (XRD) patterns of CVD SiC deposited in a temperature range of 1000 to 1300°C. Detailed analyses of the X-ray results indicate that the deposits are pure silicon carbide mainly composed of β-SiC (cubic 3C crystal structure) with a small amount of α-SiC (hexagonal 4H crystal structure). It is clear from the figure that the diffraction angles of 35.6°, 41.3°, 60.1°, 72.1° and 75.5° correspond to β-SiC and the diffraction angle of 33.7° corresponds to α-SiC. As the deposition temperatures decrease, the deposits become poorly crystallised because the diffraction peaks become broader or its intensity shown in Y axis become lower. At the deposition temperature of 1000°C, the deposits are in a quasi-amorphous state.

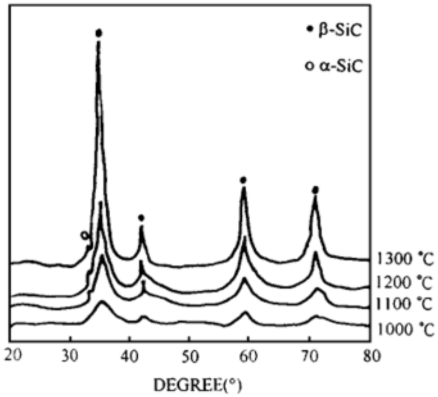

Figure 6.8. XRD patterns of CVD SiC at various temperatures [24]

Figure 6.9 shows the microstructures of CVD SiC grown at different parameters on a graphite substrate. The images on the left-hand side show a cross-section of the deposit at different temperatures, whereas the images on the right-hand side show the surface morphology of the corresponding coatings. At relatively low deposition temperatures (1000°C), the deposits are composed of a large number of spherical particles forming a cloud cluster-like structure with a smooth domed top. It should be pointed out that each particle is an aggregate consisting of a large number of nanometer SiC crystallines rather than one single crystallite. Among these particles, coalescence is clearly observed. As the deposition temperature is increased to 1100°C, the particles become larger than those deposited at 1000°C. From the microstructure cross-section, it is observed that the deposited film becomes denser. When the deposition temperature is higher than 1200°C, the size of particles is increased and the deposits become even denser.

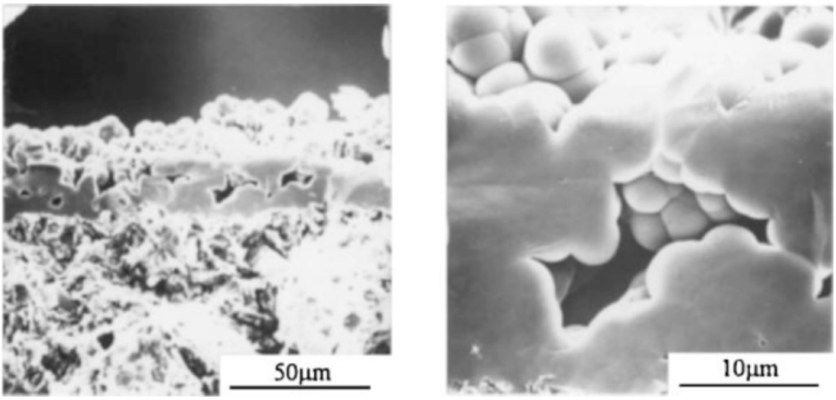

(a)

Figure 6.9. Microstructures of CVD SiC grown on graphite substrate [24]: (a) T_{dep}=1000°C, (b) *Tdep* = 1100°C, (c) T_{dep}= 1200°C and (d) *Tdep* = 1300°C

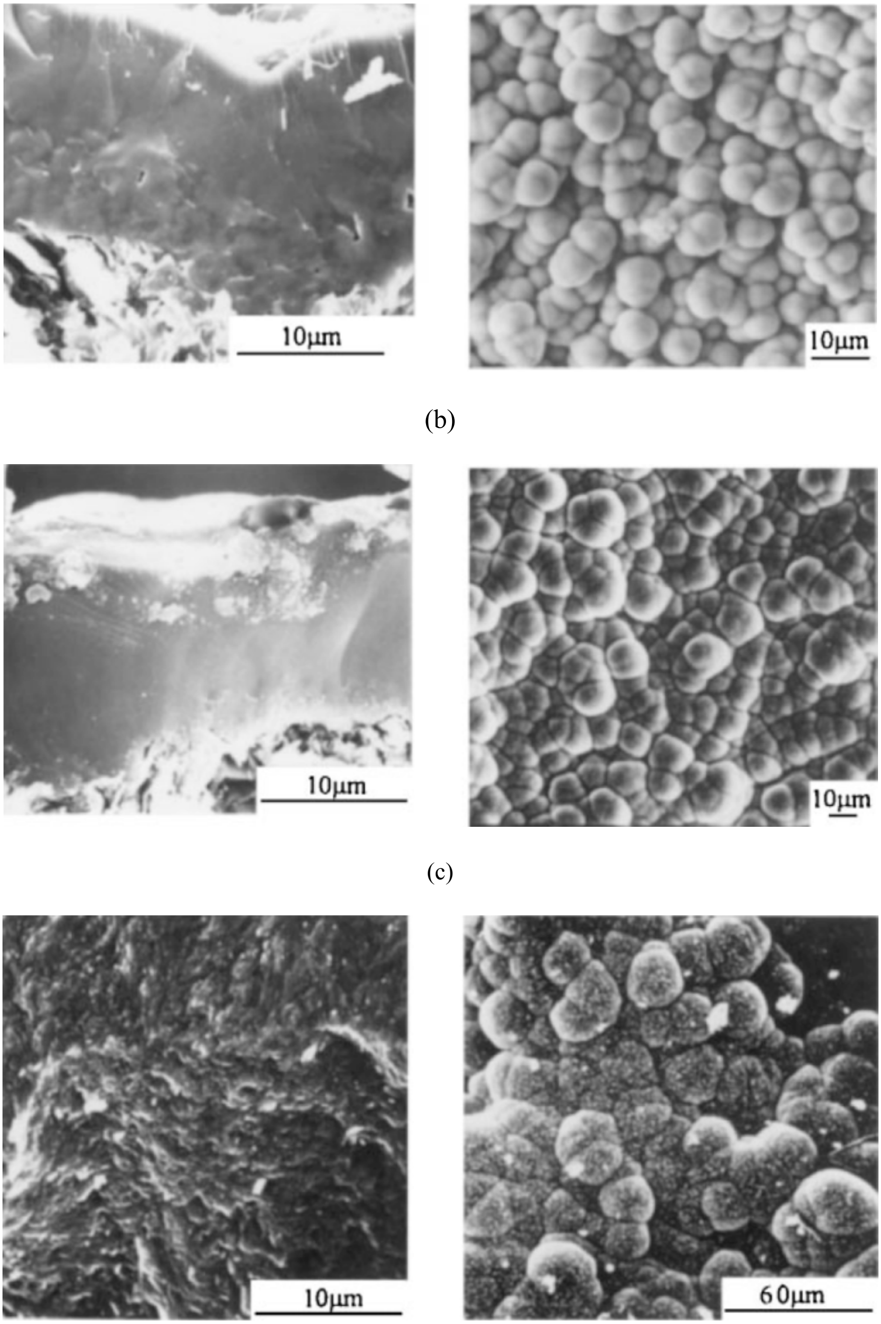

(b)

(c)

(d)

Figure 6.9. (continued)

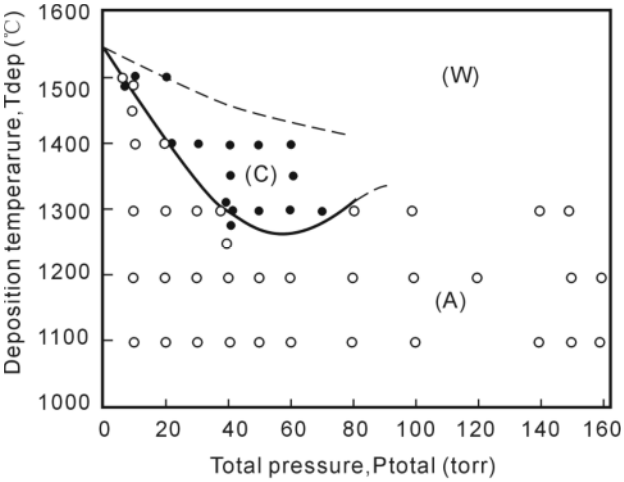

Figure 6.10. Effect of the deposition temperature and total pressure (P_{tot}) on the structure of Si_3N_4 [25]

6.2.2.3 Microstructure of Chemical Vapour Deposition Si_3N_4

As shown in Figure 6.10, both amorphous and crystalline Si_3N_4 deposits can be obtained from $SiCl_4$-NH_3 systems. These crystal structures depend markedly on the deposition temperature (T_{dep}) and the total pressure (P_{tot}) within the reaction chamber. At temperatures below 1200°C, amorphous deposits are formed over the whole range of pressures (region A). The maximum thickness of an amorphous deposit is 4.2 mm. At 1300°C, the deposit is amorphous at P_{tot} below 40 Torr and above 75 Torr, whilst a crystalline structure is formed at P_{tot} between 40 and 75 Torr. At 1400 and 1500°C, crystalline deposits are obtained between 20 and 60 Torr and between 5 and 10 Torr respectively (region C). The maximum thickness of the crystalline deposit is 4.6 mm.

According to the morphological characteristics, the amorphous deposits of Si_3N_4 may be divided into three types:

Pebble Structures

Figure 6.11a shows a typical surface structure formed at a relatively low temperature (1200°C) and low pressure (10 Torr). Only the primary pebble structure can be observed in the deposits.

Large Primary Cone Structures

Figure 6.11b shows cone structures formed at a temperature higher than 1300°C and total pressures at 30 Torr, which corresponds to region A in Figure 6.10. In this case, large primary cones are composed of secondary cones.

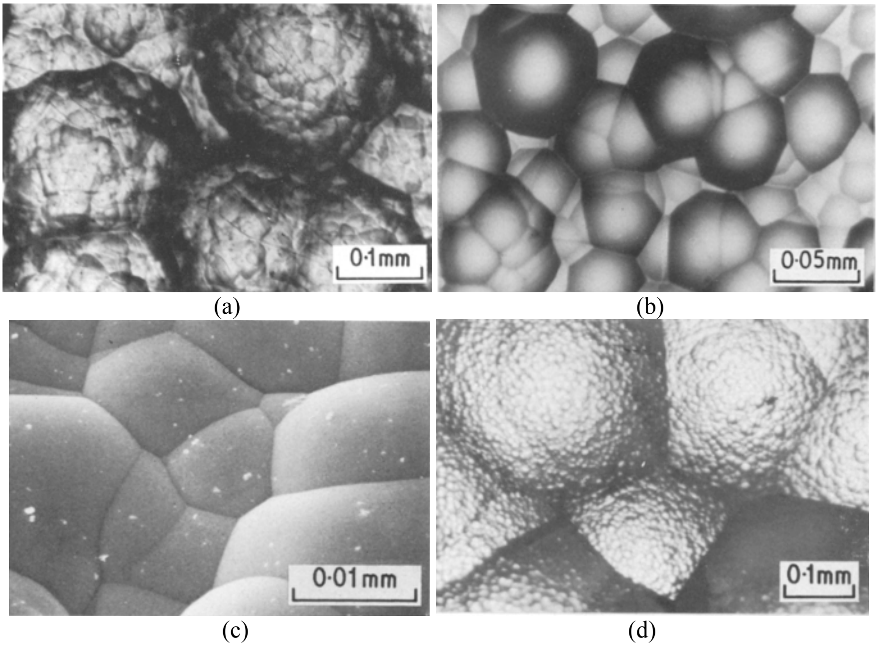

(a) pebble structure, (b) large primary cone structure, (c) and (d) large primary and second cone structure

Figure 6.11. Morphology of amorphous Si_3N_4 [25]: (a)1200°C, 10 Torr (b) 1300°C, 30 Torr (c) 1400°C, 20 Torr and (d) 1400°C, 20 Torr

Large Primary Cones and Second Cone Structures

Figure 6.11c and d indicate the third typical surface structure which is found in amorphous deposits prepared at a deposition temperature of 1400°C and pressure of 20 Torr. Large primary cones containing numerous small secondary pebble-like cones were formed. The surface of secondary cones is smooth and similar to that in Figure 6.11a.

The crystalline deposits show remarkable brightness resulting from a preferred orientation of grains. Surface structures of crystalline deposits are significantly different from those of amorphous deposits. The microstructure characteristics of the crystalline deposits are strongly dependent on the deposition conditions, as shown in Figure 6.12a–c.

At a deposition temperature of 1300°C, surface structures vary with the total pressure. At a total pressure of 50 Torr, growth cones are observed (two cones in Figure 6.12a) and each cone consists of a number of small crystals which have well-defined corners (around 90°). At a total pressure of 60 Torr Figure 6.12b, no growth cones are found and the whole surface is made up of well-grown crystals with clear prominent profiles. The surface of each crystal is very smooth. It is

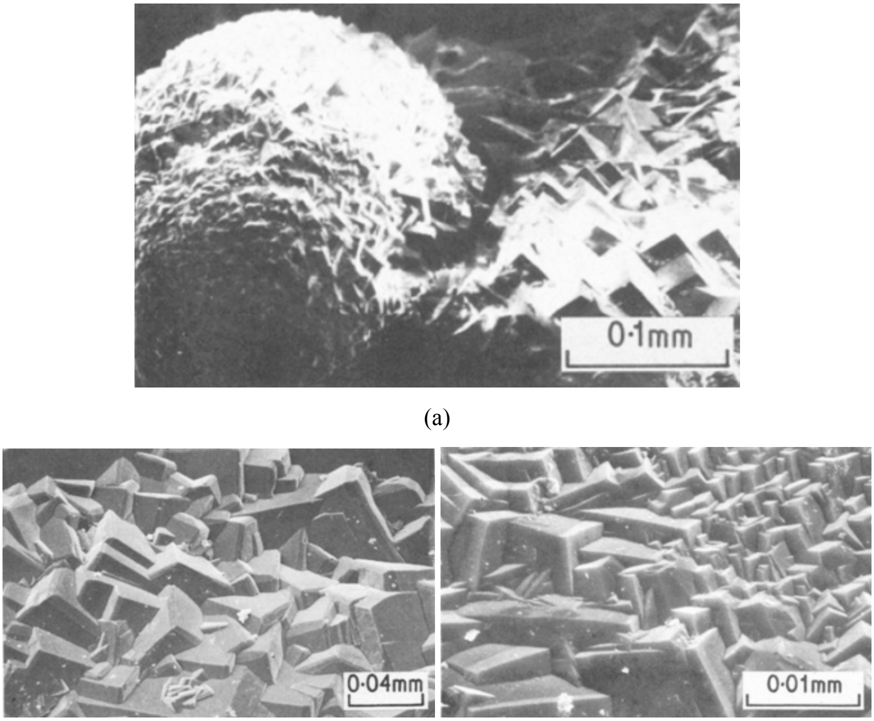

(a)

(b) (c)

Figure 6.12. Morphology of crystalline Si_3N_4 [25]: (a)1300°C, 50 Torr, (b) 1300°C, 60 Torr

obvious from Figure 6.12b that faceted growth occurs and that each grain has nearly the same orientation. At 1400°C and 50 Torr, Figure 6.12c reveals a different type of crystal growth in which another crystal face exists at the edge of almost each small crystal.

As calculated by Lespiaux *et al.* on a CH_3SiCl_3-H_2 system, supersaturation in a CVD SiC process is extremely high (more than 10^4) [12], and the nucleation and growth of the film take place at a state which is far from thermodynamic equilibrium. The morphology of the film produced in this condition can be explained by the theory of dissipative structure by Prigogine [26]. The growth mode of a CVD film is controlled not only by interface energies but also by supersaturation. Under such circumstances, the self-assembly or self-organisation of crystals is one of the key characteristics in Prigogine's theory. Self-organisation is a process of attraction and repulsion in which the internal organisation of a system, normally an open system, increases in complexity without being guided or managed by an outside source.

Cauliflower structures and conical structures are usually observed from the CVD processes as shown in Figure 6.13. Generally speaking, the former is formed by a competition between randomly branching structures, and the conical-like column is the result of continuous and inherent competition in the evolution of the

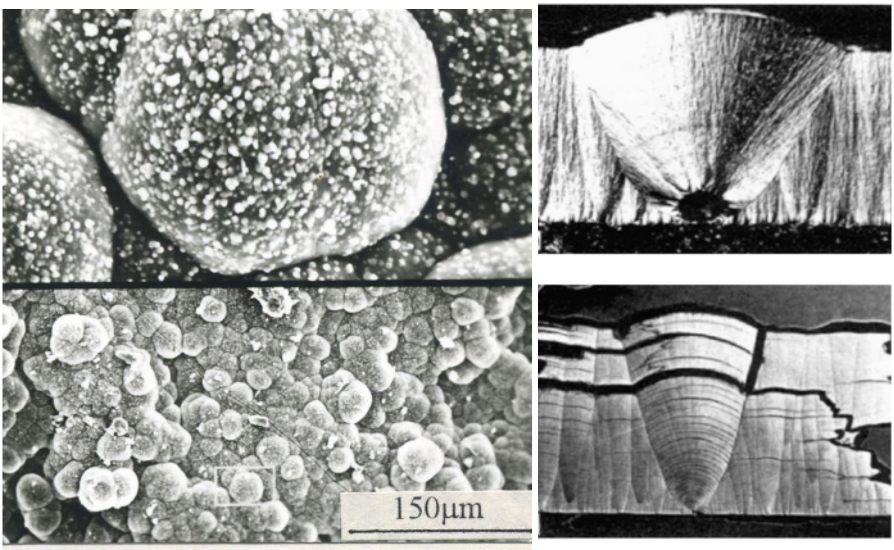

(a) (b)

Figure 6.13. Fractal structures in CVD deposits: (a) cauliflower structure and (b) conical structure [28]

physical structure [27]. The large columns are seen to be parabolic-like in profile with an internal structure consisting of small columns. Both kinds of deposits show the feature of self-similarity and are fractal structures which could be found in natural plants, such as lotus leaves. However, the evolution mechanisms for the structures are not yet understood.

6.3 Quantitative Control of Chemical Vapour Deposition Process Parameters

6.3.1 Quantitative Control Method Based on Chemical Reaction Mechanism

6.3.1.1 Free Volume Fraction and Critical Residence Time

From the CVD mechanism shown in Figure 6.14, the chemical reactions in the gas phase are much more complicated because the precursor often undergoes complex homogeneous gas-phase reactions, which result in many complex intermediate species. At the same time, the homogeneous reactions compete with heterogeneous surface reactions. The residence time, which is the duration of reactant gases flowing through the reaction, has a strong influence on the interactions of these reactions for the CVD processes.

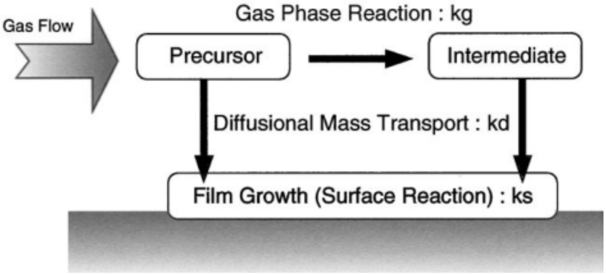

Figure 6.14. Simplified reaction mechanism of a CVD process [29]

Chemical Vapour Deposition WSi_x from WF_6-Si_2H_6

In order to identify the reaction scheme, tubular reaction experiments were used to analyse the compositions of WSi_x film from WF_6 and Si_2H_6 systems by Saito and Shimogaki *et al.* [30–32]. Figure 6.15a shows that the content of Si in the deposit of WSi_x increases significantly with an increase in the axial distance if the deposition temperature is higher than 180°C. Based on these results, the consecutive reaction model shown in Figure 6.15b was developed. It is assumed that the initial reaction forms WSi_2F_5, followed by consecutive Si_2H_6 insertion reactions to form $WF_{6-x}(SiH_3)_x$ as the residence time increases.

Chemical Vapour Deposition Cu_2O from CuI-O_2

Figure 6.16 shows an example of CVD Cu_2O from CuI-O_2. Initially, a dense film is formed as the growth rate increases due to an increase in the axial position. The

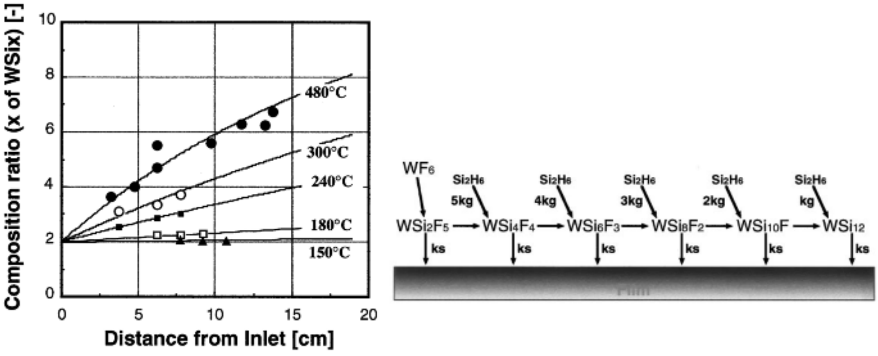

(a) (b)

Figure 6.15. CVD from WF_6- Si_2H_6 in tubular reaction [29]: (a) WSi_x CVD film composition profile and (b) reaction mechanism of WSi_x deposition

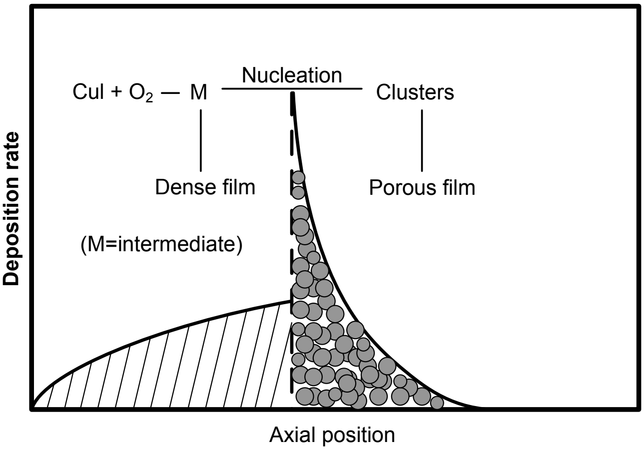

Figure 6.16. Schematic of Cu_2O deposition mechanism from CuI-O_2 system [33]

gas-phase homogeneous reactions form intermediate products that control the growth process. The deposition rate increases suddenly such that the film formed becomes porous if the film is located at a critical distance from the reaction inlet. The diameter of molecular cluster is about 1 to 2 nm, which is significantly larger than that of an intermediate molecule. This indicates that the growth mode has been changed from intermediate-molecule-based deposition to cluster-based growth. From this it can be concluded that homogeneous nucleation causes the shift from chemical-reaction-limited to mass-diffusion-limited film growth, and consequently from a dense to porous film.

Chemical Vapour Deposition Pyrolytic Carbon from CH_4

As another example, Huttinger [34, 35] has developed a synthesis reaction model based on experiments. This section introduces the work to illustrate the complex reactions and demonstrates the relationship between the chemical reactions and residence time.

For the CVD process of pyrolytic carbon from methane, the elementary reaction processes are illustrated in Figure 6.17. The following assumptions are made to discuss this scheme:

- The substrate inside a tubular reaction is heated from the outside of the wall.
- The methane temperature before entering the deposition zone is assumed to be too low to activate any chemical reactions. It is heated to the reaction temperature immediately once it enters the deposition zone.

The primary reaction of methane is the formation of the methyl radical CH_3, indicated as C1 species, according to the following reaction [34, 36]:

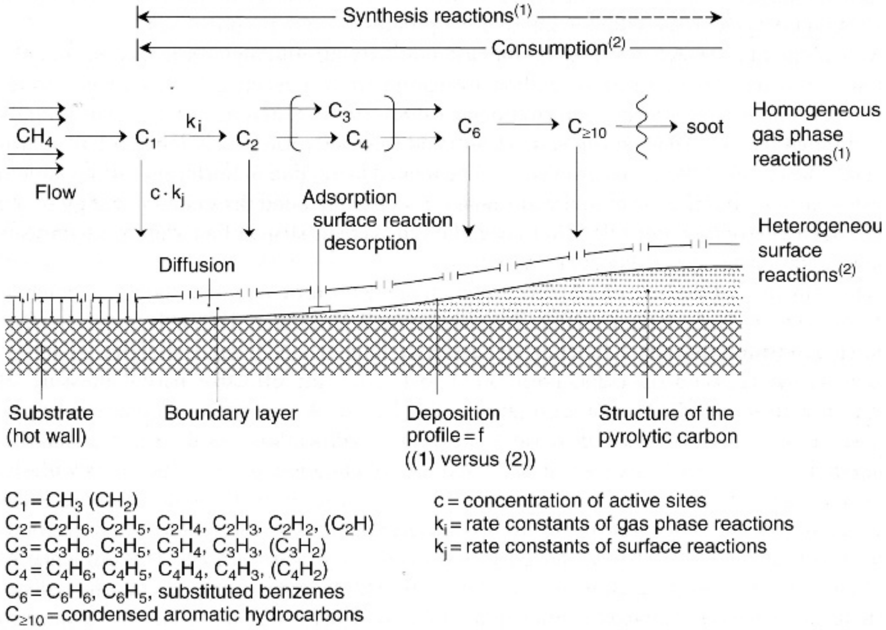

Figure 6.17. Scheme of elementary reactions in pyrocarbon deposition from CH_4 [35]

$$CH4=CH_3+H \tag{6.3}$$

$$H+CH_4=CH_3+H_2 \tag{6.4}$$

$$CH_4{}^*+M=CH_3+H+M^* \tag{6.5}$$

where $CH_4{}^*$ is the excited molecule and M is the inert gas molecule. Equation (6.3) determines the chemical reaction rate due to the high bond dissociation energy of the C–H bond.

Though methane exhibits a very low sticking coefficient, the methyl radical is supposed to be the first species that can be chemically absorbed on a substrate surface. Chemisorption takes place on an available free active site on the growing substrate surface. If such a site is not available, the methyl radical undergoes gas-phase reactions. Synthesis reactions with CH_3 become the considerations of the above reactions. Possible reactions are expressed in the equations below, and their reaction products are C_2H_6, C_2H_5, C_2H_4, C_2H_3 and C_2H_2, summarised as C_2 species.

$$2CH_4=C_2H_6+H_2 \tag{6.6}$$

$$CH_3+CH_4=C_2H_6+H \tag{6.7}$$

$$2CH_3=C_2H_6 \tag{6.8}$$

$$CH_3+C_2H_6=CH_4+C_2H_5 \tag{6.9}$$

$$CH_3+CH_4=C_2H_5 \tag{6.10}$$

$$C_2H_6=C_2H_4+ H_2 \tag{6.11}$$

$$C_2H_5=C_2H_4+H \tag{6.12}$$

$$CH_3+C_2H_4=CH_4+C_2H_3 \tag{6.13}$$

$$C_2H_3=C_2H_2+H \tag{6.14}$$

$$C_2H_4=C_2H_2+H_2 \tag{6.15}$$

$$M+C_2H_2=M+C_2H_2^* \tag{6.16}$$

The species in the above equations have the same reaction possibilities as discussed in the case of methyl radicals (CH_3). In relation to chemisorption, species with a high carbon/hydrogen ratio such as acetylene or vinyl radical react more easily. Acetylene shows a particularly strong capability of chemisorption and can even form a complex surface of carbon/hydrogen (C(H)) for blocked carbon edge atoms. On the other hand, such species are also highly reactive in homogeneous gas-phase reactions. Consequently, there is a competition between chemisorption and homogeneous gas-phase reactions of C_2 species, which has become a focus of study for the methyl radical.

As shown in Figure 6.17, the longer the residence time is, especially after the formation of C_4 species, the more likely the C_6 species or even soot will be formed. C_6 species may include benzene, a phenyl radical, or similar six-membered ring species. If the methane stays in the reaction long enough, the reaction sequence in the gas phase is terminated with C_6 species as shown in the following equations:

$$C_2H_2+ C_2H_2^*=C_4H_4^* \tag{6.17}$$

$$2C_2H_4=C_4H_8 \tag{6.18}$$

$$C_4H_4+C_2H_2=C_6H_6^* \tag{6.19}$$

$$3C_2H_2=C_6H_6 \tag{6.20}$$

$$C_4H_8+C_2H_4=C_6H_{12} \tag{6.21}$$

$$C_6H_{12}=C_6H_6+3H_2 \tag{6.22}$$

As polynuclear aromatic hydrocarbons show a high tendency towards undesired gas-phase nucleation and soot formation, they should be avoided by choosing a suitable critical residence time and other appropriate processing parameters.

After a certain residence time or reaction length the deposition profile shows a decrease in the layer thickness because of the consumption of carbon from the gas phase used in the initial range of the deposition zone. Carbon concentration, which is defined as gas-phase concentration, gradually decreases as CVD takes place from the time that the methane enters the deposition space.

The above gas-phase reaction is a polymerisation process which causes deviation from linear kinetics. Long residence-time performance is essential in large industrial reactions for forming hard coatings, where the residence time of the feed precursor is measured in minutes, whereas typical residence times for small tubular reactions is on the order of 1 s or less.

Residence time (t_r) is defined as the average time that a gas stays in the reaction chamber and is given by [37]

$$t_r=\frac{V_f}{F_{vap}\times(T/T_0)\times(P/P_0)} \tag{6.23}$$

where F_{vap} is the precursor flow rate expressed in standard conditions at a pressure of 1 atm and a temperature of 25°C, in standard cubic centimetre per minute (sccm, $ml\cdot min^{-1}$). P and T are the mean pressure and temperature in the reaction chamber respectively. V_f is the free volume within the reaction chamber.

From the above three examples, it is clear that when the chemical reactions reach a certain stage or are at a certain distance, there will be a significant change in the state of the depositions. For CVD WSi_x from the WF_6-Si_2H_6 system as shown in the first case, when the distance of the substrate is beyond a critical value, the content of Si in the deposit of WSi_x is significantly increased. For case 2, where Cu_2O is formed from CuI-O_2, an increase in the axial position results in a change of dense film to porous film. For the third case in 3, once the residence time reaches a certain level, undesired gas-phase nucleation and soot formation take place for polynuclear aromatic hydrocarbons. All these indicate that residence time at a critical level is a key consideration in the design of CVD processing parameters. Though it appears for cases 1 and 2 that distance is a key factor, they are ultimately linked to the residence time and have been used as a more convenient measure to determine the residence time.

6.3.1.2 Deposition Pressure and Surface Area and Free Volume Ratio

As discussed in Chapter 4, both homogeneous and heterogeneous chemical reactions occur in a CVD process. Within porous fibre preforms, two types of reactions are competing or interacting with each other, thereby influencing the deposition rate within the preform. Based on these understandings, Huttinger [34] proposed that a ratio called the A/V ratio should be considered as an important parameter for CVI processes. Here, A and V stand for the surface area and free volume within the porous preform, respectively. In order to investigate the influence of the A/V ratio on deposition kinetics, a special small reaction is designed and shown in Figure 6.18a. Cordierite ceramic honeycomb is used as the deposition substrate and placed into the deposition chamber made of alumina ceramic. The honeycomb structure is made of orderly arranged small pores, and this structure is used to simulate a fibre preform. Four types of ceramic honeycombs are used, and their cross-sections are shown in Figure 6.18b. Their A/V values are 0.79, 1.6, 3.2 and 7.4 mm^{-1} respectively.

Figure 6.19a shows the relationship between the deposition rate and pressure under different A/V ratios. At the low part of the honeycomb substrate, the deposition rate increases as the pressure increases below 20 kPa for all A/V ratios, then remains nearly constant between pressures of 20 to 30 kPa. It increases linearly above pressures of about 30 kPa. These different depositions rates are a result of the different deposition mechanisms in terms of the dominance of homogeneous and heterogeneous reactions under certain conditions. Under a lower

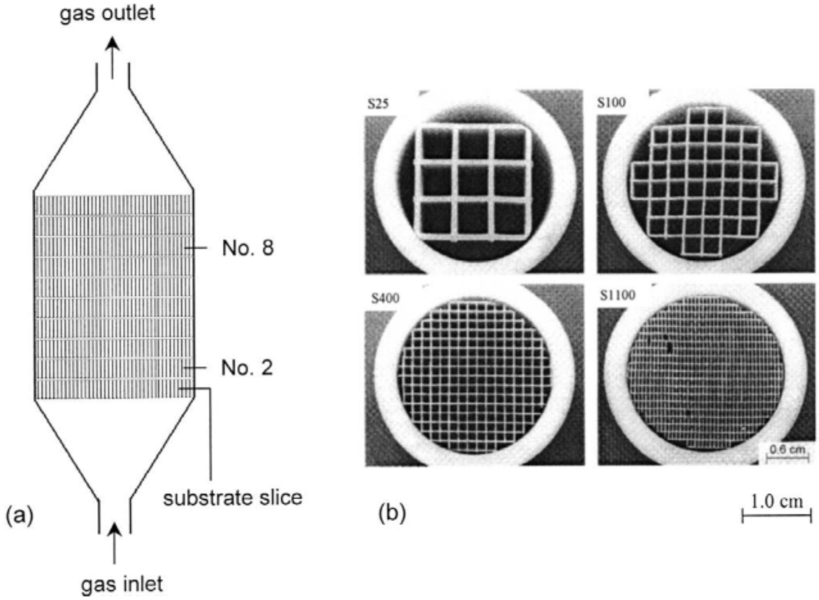

Figure 6.18. Schematic of the deposition reaction [38]: (a) arrangement of substrate slices and (b) cross-sections of substrates

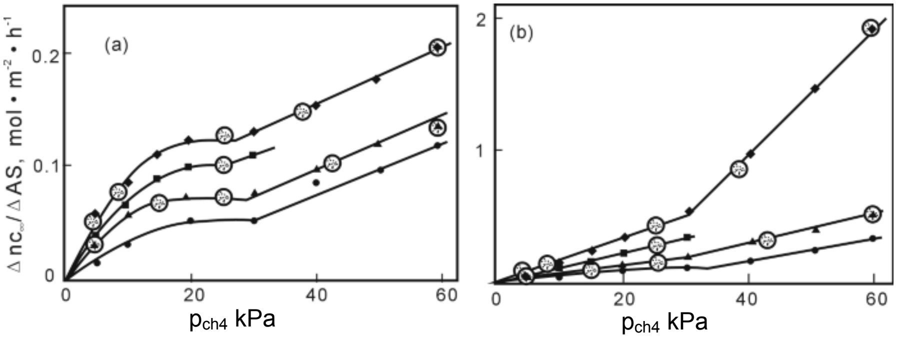

(a) (b)

Figure 6.19. Deposition rates as a function of methane pressure at a temperature of 1100 °C and various A/V ratios, [*A*/*V*] ratios of the substrates of 0.79 mm^{-1} (♦), 1.6 mm^{-1} (■), 3.2 mm^{-1} (▲) and 7.4 mm^{-1} (●) [38]: (a) lower part of the substrate and (b) upper part of the substrate

pressure, the absorption of the precursor is dominant, which implies the heterogeneous reactions on the surface play a much more important role in the deposition process. The amount of the absorbed species on the substrate increases with pressure according to the Langmuir–Hinshelwood isothermal adsorption discussed in Section 4.3. The deposition rate in a pressure range of 20 to 30 kPa corresponds to the saturated pressure. If the pressure is further increased, the absorption is not the only decisive factor for the deposition. In such a case, homogeneous reactions are also enhanced to form large gaseous species in the gaseous phase, hence the deposition rate is also further increased. The pore volume increases with a decrease in the A/V ratio. For the case of a bigger pore volume, it is more likely for the homogeneous reactions to form species with large structures (such as polycyclic aromatic hydrocarbons), hence resulting in more rapid deposition. At the upper part of the honeycomb substrate of the down stream, the deposition rate exhibits similar behavior. However, the deposition rate in the upper part of the chamber is one order of magnitude higher than that in the lower part. This implies that the role of homogeneous reactions becomes much more significant in the down stream region or the upper part of the chamber as shown in Figure 6.19b.

6.3.1.3 Sticking Coefficient

Only when the gaseous species are adsorbed on the substrate surface can heterogeneous chemical reactions take place. The amount of the gaseous species adsorbed on the substrate surface mainly depends on the sticking coefficient. The sticking coefficient (Sc) is defined as the ratio of the number of gaseous molecules and radicals in the gas phase colliding with the substrate surface and being chemisorbed for heterogeneous reaction to the total number of gaseous species hitting the substrate surface. The expression is written as [39, 40],

$$S_C = c \cdot f(\theta) \exp(-\frac{E_a}{RT}) \tag{6.24}$$

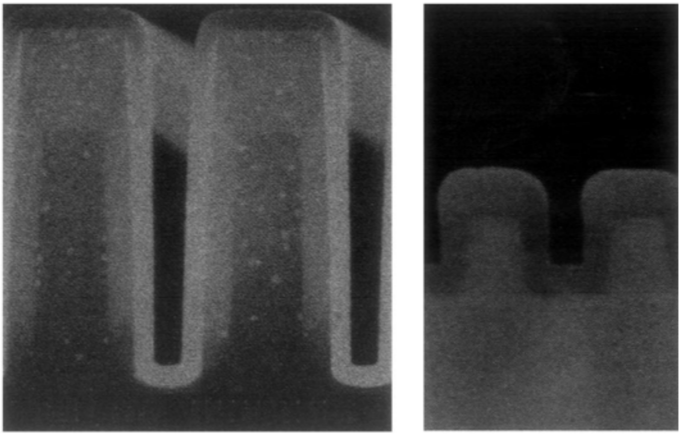
(a) (b)

Figure 6.20. Typical coverage profiles by species with different *Sc* [29]: (a) *Sc* = 0.001 for TEOS and (b) *Sc* = 0.5 for SiH_4-O_2

where *c* is the condensation coefficient, $f(\theta)$ is the fraction of available surface related to the coverage θ, and E_a is the activation energy of adsorption. *R* and *T* are the gas constant and temperature, respectively.

The *Sc* has received considerable research interest since the very early stages of fluid dynamics research, but it is still very difficult to analyse the sticking coefficients for different gaseous conditions and to determine their values [41,42]. Generally speaking, the Sc of active radicals is higher than that of the stable species. This coefficient is dependent not only on the nature of the species, but also on the processing conditions (such as temperature). Table 6.2 lists the relationship between *Sc* and temperature. The data are determined by the direct Monte Carlo simulation based on the experimental results. As the temperature increases, the coefficient significantly decreases from 0.50 to 0.08.

For the infiltration of a pore with a large aspect ratio, a small *Sc* implies the entire surface of the deep pore can be uniformly coated. The reason is that the reactant gaseous species are easily transported to the bottom of the pores by

Table 6.2. Sticking coefficient of SiH_4-O_2 at different temperatures [43]

Temperature (°C)	573	673	723
Sticking coefficient	0.50	0.24	0.08

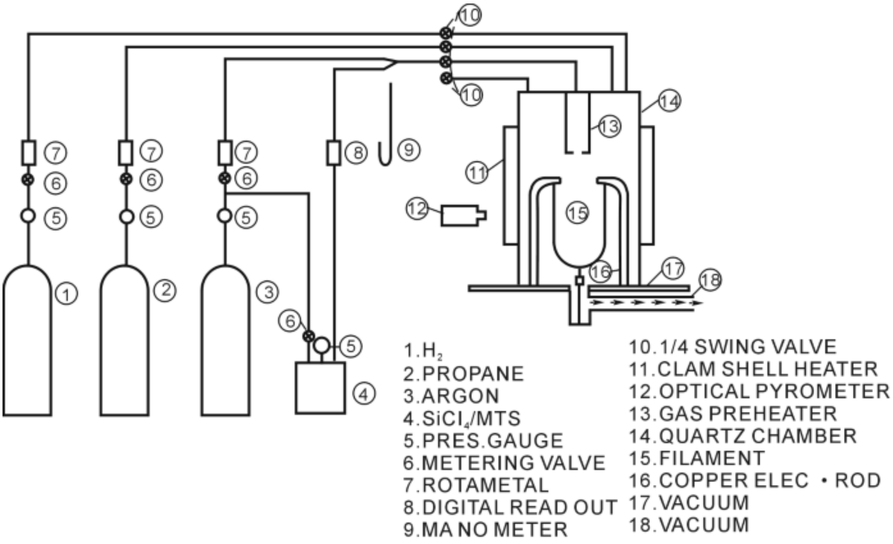

Figure 6.21. Schematic for CNTD-SiC process [44]

multiple reflections inside the wall of a pore. For a large *Sc*, however, the deposition takes place preferentially at the opening of the pore, hence resulting in poor infiltration. This is due to the fact that reactant species have a tendency to attach to the opening part of the pore.

The Sc of the tetraethyl orthosilicate ($Si(OC_2H_5)_4$-TEOS) and SiH_4-O_2 are 0.001 and 0.5 respectively. For SiO_2 deposition from TEOS, the deposition thickness is very uniform from the opening to the bottom of a micro-trench. However, the SiO_2 coating from SiH_4-O_2 at the outer location of the trench is markedly thicker than that in depth of the microtrench, even if the aspect ratio of the microtrench is much small than that for TEOS, as shown in Figure 6.20.

6.3.2 Experimental Basis for Quantitative Control Parameters

6.3.2.1 Preheat Temperature

For a cold-wall reaction with small heating source, preheating the precursor gases is preferred and important in order to obtain thick coatings with a smooth outer surface and fine crystal structure. This is normally realised by using a separately designed heater system. By contrast, precursor gases in a hot-wall reaction are always preheated before being transferred to the surface of the substrate, as mentioned in Section 3.4.

A representative example is to deposit a CVD a SiC thick coating on a tungsten wire. This CVD system, developed by Chemetal Corporation [44, 45], USA, uses tungsten wire with a diameter of 500 μm and a length of 200 mm as a substrate. The wire is directly heated by passing an electric current through it. For SiC deposition, a mixture of CH_3SiCl_3, H_2 and Ar is employed as the precursor gases.

These gases are preheated to the preset temperature in a clamshell heater before they reach the surface of the tungsten wire. The CVD process is operated within a quartz chamber as shown in Figure 6.21.

Figure 6.22a and b compare the morphology difference of the coating surface formed by conventional CVD and controlled nucleation thermochemical deposition (CNTD), which is a proprietary CVD technique. If the precursor gases are preheated, the coating surface is very smooth. However, the coating comprises a number of irregular aggregates and its surface is very rough if the conventional CVD technique is used. From a cross-sectional view, the coarse columnar structure is observed in the conventional coating shown in Figure 6.22c. For CNTD coating, the equiaxed SiC grains are very fine and their crystal sizes range from 10 to 100 nm as observed using TEM, as shown in Figure 6.22d.

The effect of preheating on growth modes and surface finishes can be explained by the nature and amount of intermediates through homogeneous reactions. If the precursor gases are not preheated, there are not enough active

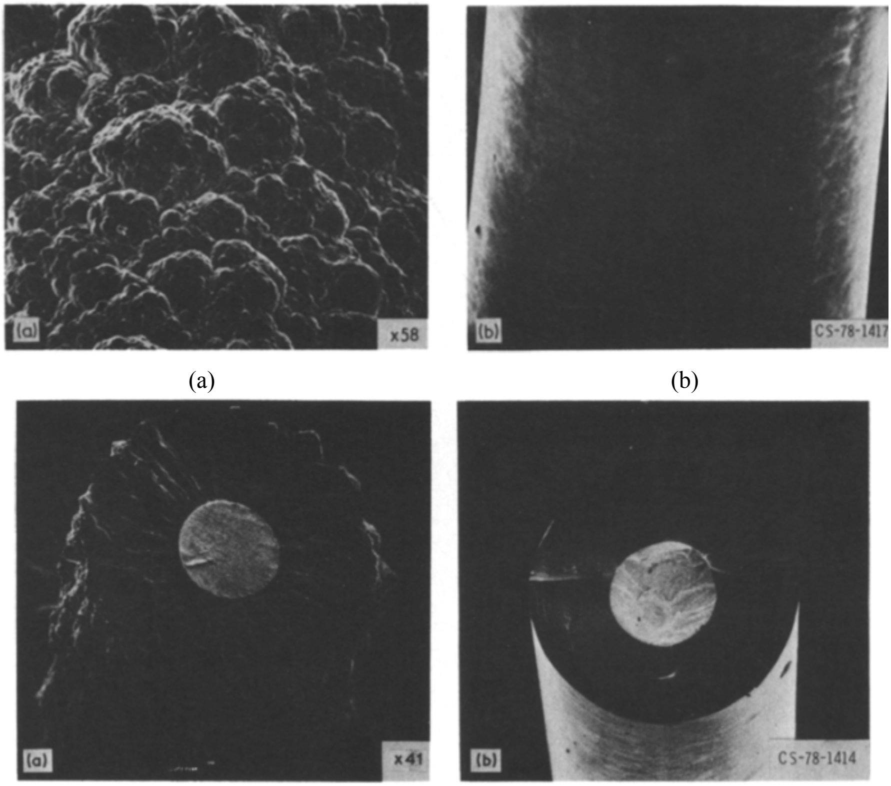

(a) (b)

(c) (d)

Figure 6.22. Microstructure of CVD SiC coating by different CVD methods [44]: (a) surface morphology by conventional CVD, (b) surface morphology by CNTD, (c) cross-section structure by conventional CVD and (d) cross-section structure by CNTD

intermediates being adsorbed onto the preferred sites (such as terrace, ledge and kink) on the substrate surface. In this case, the growth of the deposit takes place along the preferred orientation from those sites, which results in the formation of a columnar structure with coarse grains. This is very similar to the cave crystal formation process, where $CaCO_3$ water-containing runs along the rough ceiling surfaces to the lowest projected points to form drops at a low flow rate. In the course of dripping over this gradually expanding columnar structure, $CaCO_3$ is deposited on the surface to form a large columnar structure, which is called a cave crystal. If the precursor gases are preheated adequately, then enough active intermediates will be produced from homogeneous reactions. These intermediates can cover the substrate completely and be adsorbed on the substrate surface to ensure a uniform heterogeneous reaction to form the deposit with a smooth surface. In this case, the equiaxed fine grains are deposited rather than the coarse columnar grains.

6.3.2.2 Depositing Time

A number of attempts have been made and methods have been developed to improve the deposit thickness uniformity as shown in Figure 6.23. These methods include periodically reversing the gas flow direction, rotating the substrate, combining gas flow reversal and substrate rotation, stirring the gas, periodically repositioning the substrate, imposing a temperature gradient over the length of the substrate and tilting the substrate to increase its downstream projection into the boundary layer [14].

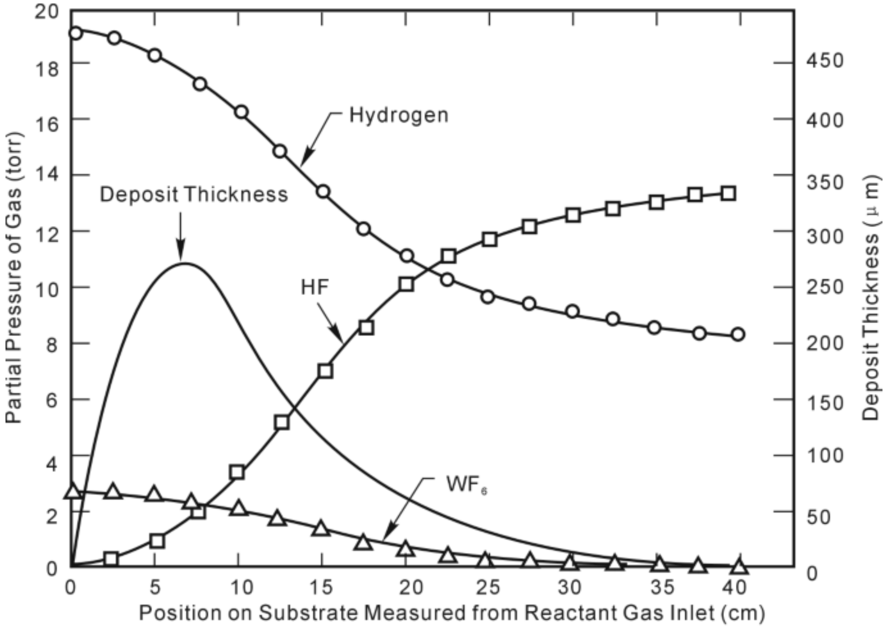

Figure 6.23. Gas composition and deposition thickness profile through the CVD process [46]

Table 6.3. Process parameters for P-CVD [46]

Deposition temperature	640°C
Nominal pressure during deposition	15 Torr
Nominal pressure during evacuation	2 Torr
Cycle time	10 s coat, 5 s exhaust
H2/WF6 ratio	6

Bryant [46] developed a novel method to fabricate a complex and large component with uniform thickness. Investigations reveal that the deposit thickness is largely dependent on the composition distribution of the reactant gases along the substrate. Figure 6.23 shows the composition variation of gases within a reaction chamber for a tungsten deposition from a tungsten fluoride and hydrogen system. As the distance to the gas inlet increases, the partial pressures of both reactant gases (WF_6 and H_2) are decrease; however, the partial pressure of the by-product of HF is increased significantly. As a result, the thickness of the deposit (*W*) is increased initally and reaches a maximum value at a distance of around 70 mm from the inlet. The thickness then decreases with distance, corresponding to the decrease of the partial pressures of the reactant gases. Pulsed chemical vapour deposition (P-CVD) was proposed to solve the reactant depletion problem and to lead to *W* deposit with uniform thickness along the length.

As indicated in Section 5.6 (pulsed CVI process), deposition time is a critical process parameter to control layer thickness uniformity and deposition quality. Unlike other traditional methods, the distinguished feature of P-CVD is that reactant gases are introduced in pulses, rather than in a continuous flow manner, into a previously evacuated deposition chamber at a high velocity. Tungsten deposition is conducted by repeated cycles of gas injection followed by chamber evacuation, forming pulses of gas injection into the chamber. Such a pulsing technique avoids the problem of gas composition and concentration being dependent on the position on the substrate. Instead, in pulsing, gas concentration varies as a function of time but in the same manner for every portion of the substrate. Details of the process parameters and techniques can be found in Table 6.3.

A tapered tungsten tube produced by the CVD process is shown in Figure 6.24a. Its as-deposited length is 1070 mm. The wall thickness is 0.75 mm and varies within the limits of ±0.025 mm. The inner wall surface finish is 8 rms, equivalent to the finish of the mandrel. The outer wall surface finish is about 250 rms, which is a typical value associated with fluoride-produced CVD tungsten.

The microstructure of the tube taken in a direction normal to the growth direction is shown in Figure 6.24b. The multi-layer columnar grain structure in this figure is the result of cyclically interrupted deposition because of P-CVD. The deposition rate is calculated to be 30 $\mu m \cdot h^{-1}$. This is well below the deposition rate of 125 $\mu m \cdot h^{-1}$ normally achieved with the same parameters of temperature and

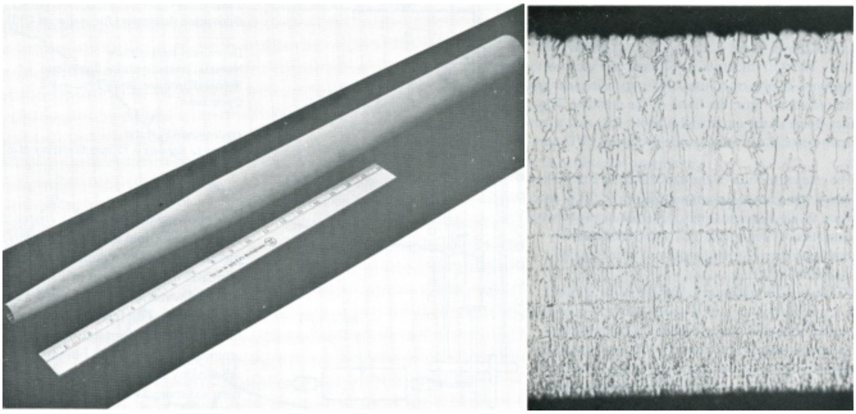

Figure 6.24. Tungsten tapered tube produced by pulsed CVD [46]: (a) a tube 1070 mm long and 0.75 mm thick (b) microstructure of W deposit

pressure when a non-interrupting flow-through process is used. The discrepancy in deposition rates can be attributed to two facts: (1) no deposition occurs during the part of each cycle used for the chamber evacuation and (2) little tungsten deposition occurs during the gas introduction phase of the deposition cycle. The latter conclusion is substantiated by the experimental observation that for each cycle the system pressure only increases for about 3 or 4 s from the time of gas injection. Increasing pressure from 10 to 80 Torr is effective for increasing the deposition rate of tungsten because there is more precursor supply for the deposition. The same increase is also observed by increasing the temperature from 640 to 750°C.

6.3.2.3 Influence of Temperature and Pressure on the Microstructure

It is well established that three types of pyrocarbon can be obtained by CVD processes, namely smooth laminar (SL) structure, rough laminar (RL) structure and isotropic (ISO) structure pyrocarbon. Their structural characteristics were first identified from optical observations by Lieberman and Pierson [41] in the 1970s.

Table 6.4. Physical and structural characteristics of three types of pyrocarbon [47]

	ISO	**SL**	**RL**
Density (g/cm^3)	1.5–1.8	1.7–1.9	2.0–2.1
Extinction angle (°)	<4	12~18	>18
Diamagnetic anisotropy	Very weak	Weak	Strong
TEM experiments	Micropores	Flattened pores	No pores
Graphitisability	No	Partial	Yes
D (002) after HTT at 2800°C (nm)	0.344	<0.344	0.337

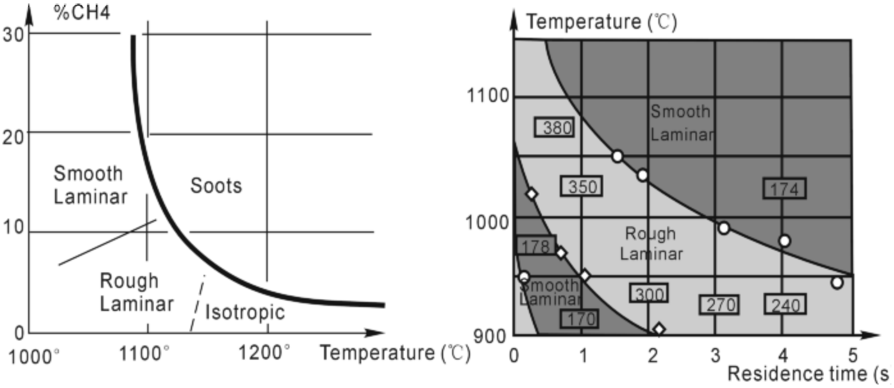

Figure 6.25. Microstructure characteristics of CVD pyrocarbon [47]: (a) influence of precursor partial pressure and temperature and (b) influence of residence time and temperature

Further investigation revealed some more differences among these three pyrocarbons, as listed in Table 6.4. A mixture of three types of pyrocarbons is always obtained in a CVD process. Of these, it is more desirable to produce RL pyrocarbon because of its high density, dense microstructure and good graphitisability. These advantages result in the superior friction behaviour for applications such as carbon/carbon braking discs and ablation resistance for thrust liners of a solid rocket engine.

For the CH_4-N_2 deposition system, the relationship between pyrocarbon structure and processing parameters is well established, as shown in Figure 6.25a. SL pyrocarbon is deposited at a high pressure of CH_4 precursor but a low temperature of less than 1100°C. By contrast, ISO pyrocarbon is obtained at a low pressure of CH_4 precursor but a high temperature of more than 1150°C. RL pyrocarbon is formed and deposited at the middle range of temperature and pressure, i.e. middle pressure and middle temperature. Soots are produced at both high temperature and high precursor pressure by homogeneous nucleation in the gas phase. In addition, the residence time of the precursor in the reaction zone plays an important role in the microstructure formation of the pyrocarbon. At a deposition temperature of 1000°C, the pyrocabron microstructure is changed from SL to rough laminar then to SL structure as the residence time increases, as shown in Figure 6.25b.

6.3.3 Quantitative Control Parameters on the Basis of Fluid Mechanics Consideration

Preforms placed in a reaction chamber are subject to gas flow and allow deposition. The gas flow patterns are governed by pressure and velocity and have a significant influence on the rate and quality of the deposit. It is essential to have a good understanding of the impact of gas flow patterns on a CVD process. This enables a suitable design solution to both preforms and gas channelling systems, including the location of preforms in the chamber and some gas flow guides if necessary, such that a high-quality deposition is achieved with a higher deposition rate. The key to achieving this is to minimise the pressure drag force.

Drag reduction of an object moving relative to its surrounding gas or fluid is a focal research point in design and analysis of such an object, such as an aircraft or a boat. Such a drag mainly depends on the shape of the object for a given flow. Rain droplets are good examples of the shape with the smallest drag coefficient when they fall in air. Their shape possesses excellent aerodynamics with a rounded front and a slim rear. This type of aerodynamic form is critical to any object when it travels in a fluid, whether a high-speed aircraft or a fish swimming in water. By designing and arranging the preforms in a reaction chamber, it is possible for them to present the smallest possible drag coefficient and reduce the residence time of the precursor gases within the reaction chamber.

6.3.3.1 Boundary Layer Separation

For a flat plate in a gas stream flow, arranged with its flat surface aligning along the flow direction, the streamline pattern is hardly affected by the presence of the thin boundary layer of the plate and remains nearly straight and parallel. The uniform pressure of the outside boundary layer does not affect the streaming flow which is impressed on the boundary layer flow. As a consequence there are no pressure variations either across or along the boundary flow. For a part with a curved surface or profile, the streamline flow and the pressure change are different from those of a flat plate [48]. The fundamental difference between flow over a flat plate and flow over a curved surface is the pressure variation caused by the curved surface. The flow is commonly divided into three zones, as shown in Figure 6.26, determined by the pressure change.

Pressure Decrease Zone

In the case where a gas flows over the front portion of a curved surface or a convex curve surface, the flow outside the boundary layer accelerates. The boundary layer over most of the front portion remains fairly thin and has a uniform streamline pattern over this portion. According to the Bernoulli equation [48], accelerated flow results in a pressure decrease in the vicinity of the front portion area. In this zone, the pressure gradient is positive, i.e. the direction of pressure gradient is the same as the flow direction. The positive pressure gradient is helpful to push the flow within the boundary layer forwards. The variations of velocity and pressure are expressed as

$$\partial u_x / \partial x > 0 \tag{6.25}$$

$$\partial P / \partial x < 0 \tag{6.26}$$

Top Point

At the top point of the curved surface, the flow is accelerated to the maximum value, however, the pressure reaches the minimum value. This means

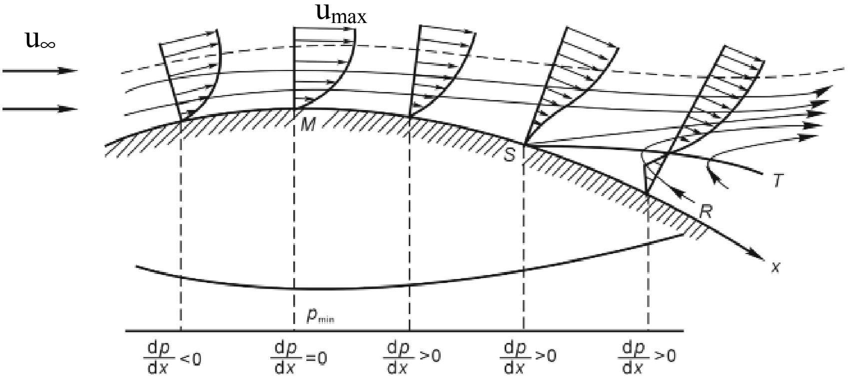

Figure 6.26. Boundary layer separation of a flow over a curved surface

$$\partial u_x/\partial x = 0 \tag{6.27}$$

$$\partial P/\partial x = 0 \tag{6.28}$$

Pressure Increase Zone

In the flow over the back portion of the curved surface as shown in Figure 6.26, the flow begins to decelerate, causing in the pressure of the outside flow. The flow in the boundary layer also decelerates because of the viscous resistance within the boundary layer and reverse pressure gradient outside the boundary layer. Finally, at some location along the back side of the curved surface, part of the boundarylayer flow stalls, or comes to rest. The increasing pressure then causes this stalled flow to reverse direction and flow back along the curved surface. This phenomenon is called boundary layer separation and the region of reversed eddying flow is called the wake.

In this zone, the velocity and pressure variations are expressed as

$$\partial u_x/\partial x < 0 \tag{6.29}$$

$$\partial P/\partial x > 0 \tag{6.30}$$

6.3.3.2 Profile Drag Coefficient

The separated boundary layer and wake displace the outside streamline pattern, which causes the pressure distribution to be significantly altered. Boundary layer separation causes a force on the body called drag force. The drag coefficient is defined as the ratio of total profile drag force divided by the flow pressure and projected area of an object and is expressed as [49]

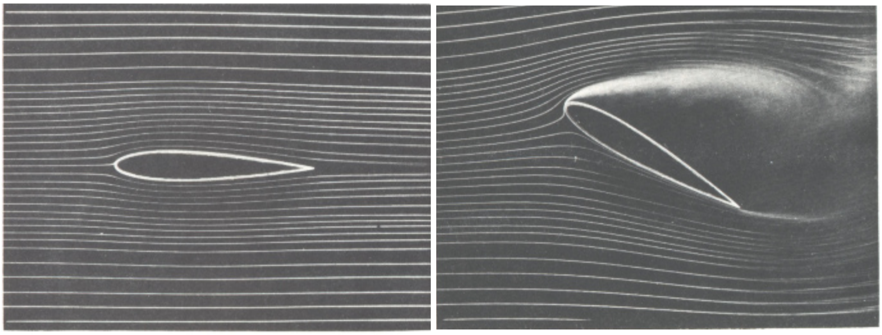

(a) (b)

Figure 6.27. Orientation of an airfoil on the drag force [50]: (a) zero angle of attack and (b) large angle of attack

$$C_D = \frac{F_D}{A_p \rho u_0^2 / 2} \tag{6.31}$$

where A_p is the projected area of a body, ρ is the fluid density, u_0 is the free stream velocity, and F_D is the drag force usually determined by experiments.

The drag coefficient (C_D) can be determined if the pressure and shear stress distribution around a body are known. The drag coefficient can also be calculated if the total drag is measured, for example, by means of a force dynamometer in a wind tunnel. Then C_D is calculated using the above equation.

The drag force contributed by pressure drag and friction drag to the profile drag strongly depends upon the shape of the body and its orientation with respect to the flow of the fluid. For instance, if an airfoil is placed in a fluid stream with zero angle of attack, as shown in Figure 6.27a, the pressure drag is negligible, because even though the pressure recovery is incomplete, the resulting pressure difference acts on a very small frontal area (perpendicular to the flow). The skin friction drag, however, is substantial, owing to the formation of the boundary layer on the surface of the airfoil. If the angle of attack is large as shown in Figure 6.27b, the drag force also becomes very large due to the pressure difference, whereas the skin friction drag is negligible.

The drag coefficient is not only related to the shape and orientation of an object, as shown in Figure 6.28, it is also affected by the Reynolds number (Re) of the flow gas. This can be explained by inserting this statement into the definition of Reynolds number in Equation (2.58). The thickness of the boundary layer is decreased as the Reynold number increases, therefore reducing the contribution of the velocity boundary layer to the drag force.

6.4 Numerical Design and Analysis Techniques for Flow Field

Expanding on the introduction of a proposed engineeirng design approach in Chapter 3, this section describes a specific and effective approach to facilitating the design of a CVD or CVI system and its associated process control parameters. As an effective and rapid evaluation method, computational fluid dynamics (CFD) has developed significantly and has been widely used in recent years [51, 52]. Whilst there are many commercially available CFD software tools, such as CFX, PHOENICS, I-DEAS-ESC, FLUENT, FLOW3D and STAR-CD; their applciations have been fully explained in other publications. Therefore the focus of this section is not to give a full theoretical introduction to the technique. This section aims to give a brief introduction to CFD theory and problem solving techniques and, more importantly, how one can use the techniques effectively in a real CVD system design. Some example CFD uses in solving CVD problems are also demosntrated.

CFD-based techniques date back to the early 1960s, and the first commercial CFD software became available in the early 1980s. Since then, research and development into CFD has transformed the techniques from a theoretical approach

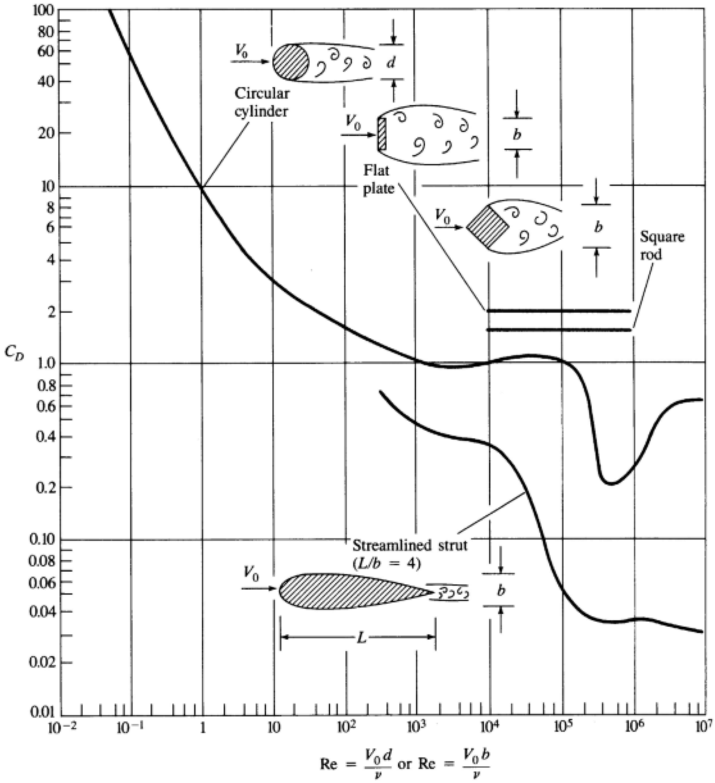

Figure 6.28. Drag coefficient vs. Reynolds number for two-dimensional bodies [49]

into a very effective and useful tool for many practical engineering problems. This is especially the case over last 10 years due to significant improvements in the computer user interface, as well as to rapid advancement in computational powers of personal computers. This effectively enables many engineers and graduates to model a particular system involving physical phenomena such as single or multiphase fluid/gas flow, flow turbulence, chemical reactions and radiative heat transfer that cover aerospace, chemistry, marine meteorology and a wide range of industrial and non-industrial application areas. Complex applications such as gas flow in a CVD system, aero dynamic race car design, aerofoil design in aeronautics, rocket modelling and simulation in aerospace drag simulation in automobile design, jet and thermal flow in engine design, and lava flow simulation in earthquake study can all make use the CDF methodology. This is beacuase complex geometric representations of components or systems have been significantly improved. The performance of problem solving and visualisation have also been greatly enhanced.

Similar to other computer simulation techniques, CFD-based tools enable CVD system designers to undertake many what-if scenario studies to evaluate and assess the impact of design decisions on a system and on components manufactured by CVD or CVI in a virtual computer environment. This can greatly reduce the cost and time associated with traditional trial-and-error methods used in designing such sophisticated CVD systems and their process control parameters. For studies of complex multiphysics processes such as those taking place in a CVD process, CFD can provide an ideal environment in which many multiphysics phenomena can be investigated. This in turn reduces the cost associated with system design and process parameter determination by experiments. It can potentially help designers come up with a CVD design solution which can produce correctly deposited components the first time. Hence, CFD enables designers to study system behaviours without real difficulty and without the use of costly experiments. It can form an integral part of a powerful computer-aided CVD design and evaluation environment.

6.4.1 Governing Conservation Partial Equations Used in Computational Fluid Dynamic Approach

Gas flow in a reaction is considered to follow the principles of conservation of momentum, energy, and total mass. These parameters are used to simulate flow behaviour through numerical solutions of differential equations. The general derivation and form of these equations are given in standard references [53–55], and these principles and related equations are briefly introduced below.

Conservation of Mass Equation

Within CFD, mass is conserved, that is the rate at which mass enters a volume element equals that mass leaving the element in any steady state process. The mass continuity equation is important and is hence developed by formulating the relationship between the mass flowing into and out of a stationary volume element:

$$Rate\_of\_mass\_accumulation = Rate\_of\_mass\_in - Rate\_of\_mass\_out \quad (6.32)$$

The above relationship defines the physical principle of continuity – mass conservation. A more concise mathematical representation of the mass conservation principle is given for a flow with a density of ρ and flowing at a speed of u by

$$\frac{\partial \rho}{\partial t} + \nabla \cdot (\rho \overrightarrow{u}) = 0 \tag{6.33}$$

where ∇ is the vector elementwise differential operator, known as the 'del' or 'nabla' operator.

Assume there is an incompressible fluid flow with a constant density ρ; the above equation can then be simplified as a very important special form of the continuity equation

$$\nabla \cdot (\overrightarrow{u}) = 0 \tag{6.34}$$

Conservation of Momentum Equation

For a CFD volume element, conservation of momentum can be expressed by the following statement:

$$R_{m\_a} \cdot = R_{m\_in} - R_{m\_out} + S_f \tag{6.35}$$

where R_{m_a} is the rate of momentum accumulation, R_{m_in} is the rate of momentum in, R_{m_out} is the rate of momentum out, and S_f is the sum of forces acting on the system.

Mathematically, the above can be expressed by the well-known Navier–Stokes equation as

$$\rho \frac{D\overrightarrow{u}}{Dt} = -\nabla p - \nabla \cdot (\overrightarrow{\tau}) + \rho \overrightarrow{g} \tag{6.36}$$

where the left-hand side represents acceleration multiplied by density or the mass per unit volume. The right-hand side is the summation of various forces on the element per unit volume from the pressure force ∇p, viscous force $\nabla \cdot (\overrightarrow{\tau})$ and gravity $\rho \overrightarrow{g}$, respectively. In a physical sense, the Navier–Stokes equation is another form of Newton's second law.

Here the partial time derivation, ∂/∂t, describes how the variable (concentration, velocity and temperature) changes with time at a fixed position. Substantial time derivation, D/Dt, is a special kind of total time derivation computed by an observer floating downstream with the fluid. In this form the equation of motion states that a small volume element moving with the fluid accelerates because of the forces acting upon on it.

For constant density gases with constant viscosity, Equation (6.36) can be simplified as

$$\rho\frac{D\vec{u}}{Dt} = -\nabla p + \mu\nabla^2 \cdot (\vec{u}) + \rho\vec{g} \tag{6.37}$$

where ∇^2 is the Laplace operator.

Conservation of Energy Equation

The conservation of energy is also called the First Law of Thermodynamics and is based on the concept that energy can be neither created nor destroyed. This conservation of energy defines the relationship between the energy involved in an isolated system and work (the mechanical energy) the system does on its surroundings. The differential equation of energy can be derived according to the physical principle of mass conservation:

$$R_{e\_a} \cdot = R_{e\_in} - R_{e\_out} + R_{ew} \tag{6.38}$$

where R_{e_a} is the rate of energy accumulation, R_{e_in} is the rate of energy in, R_{e_out} is the rate of energy out, and R_{ew} is the rate of external work done by the system on its surroundings.

The energy within a system includes potential energy, kinetic energy and internal energy. Under steady conditions, the mathematical equation for an incompressible fluid with constant properties is expressed by

$$\frac{DT}{Dt} = \alpha\nabla^2 T + \dot{q} + \mu\Phi \tag{6.39}$$

where T is the temperature, $\dot{q}$ is the rate of heat generation per unit volume, α and μ are the thermal diffusivity and viscosity coefficients respectively, and Φ is the friction heat resulting from viscous force.

If there is no interior heating source within the system, $\dot{q}$ becomes zero. Moreover, the viscous dissipation term ($\mu\Phi$) is generally negligible except where extremely large velocity gradients exist in a system. As a result, the latter terms of the right side of Equation (6.39) can be omitted and the equation can be rewritten as

$$\frac{DT}{Dt} = \alpha\nabla^2 T \tag{6.40}$$

The above conservation equations can be used to work out the profiles of concentration, temperature and velocity within the reaction chamber of a CVD process. For the most commonly used isothermal CVD systems, it is understood that the temperature and gas concentration has less influence on CVD processes than velocity. Therefore, the next section focuses on the velocity of CVD systems.

6.4.2 Computational Fluid Dynamics in Chemical Vapour Deposition

Computational fluid dynamics (CFD) is essentially a computer-based numerical analysis approach for fluid flow, heat transfer and related phenomena. CFD techniques typically consist of the following five subprocesses: geometrical modelling, geometry discretisation, boundary condition definition, CFD-based problem solving, and post-processing for solution visualisation.

6.4.2.1 Geometrical Modelling

The geometric representation of a solid object such as a CVD reaction chamber or any substrates inside the chamber can be represented unambiguously using solid modelling techniques, which is also known as volume modelling as it deals with the three-dimensional (3-D) volume of these solid objects. Within these techniques, a solid object can be represented by boundary representation (B-Rep) as a volume contained in a set of faces together with topological information which defines the relationships between the faces, vertices and edges and how they are joined together. This technique can represent a wide range of solid objects and can employ the *intersection*, *union* and *difference* techniques between two arbitrary shapes overlapping in a 3-D space to represent complex objects.

Three-dimensional objects can also be represented by so-called primitives in a constructive solid geometry (CSG) representation. These primitives are the essential building blocks of more complex shapes and include simple shapes: cuboids, cylinders, prisms, pyramids, spheres, cones and so forth. Boolean operators include *Union* to add a new primitive into an existing shape, *Cut* to subtract a particular shape from an existing shape, and *Intersect* to generate the overlapped volume. Building on these operations, complicated geometry can be created using basic objects. As each basic object contains necessary information, the processing of compound shapes is usually simpler and less demanding compared with the B-Rep methods. For CVD system modelling, some system components are of regular shapes and hence can be easily modelled using this method. Figure 6.29 shows an example of the chamber and substrates model created using this basic technique.

Wireframe models are also used in many applications and are visual representations of a physical object which only specify and display straight or curved edges at the point of intersection of two faces. Edges are connected to each other with vertices. A wireframe model is represented by tables defining edges and points. The start point and end point of each edge are stored in the edge table. An edge may be a line or a curve. The coordinates of each point are stored in the point table. A wireframe model is stored in a computer as a data structure, using very small data space. Wireframe representation is particularly useful for mesh representation in CFD and finite element analysis (FEA) techniques.

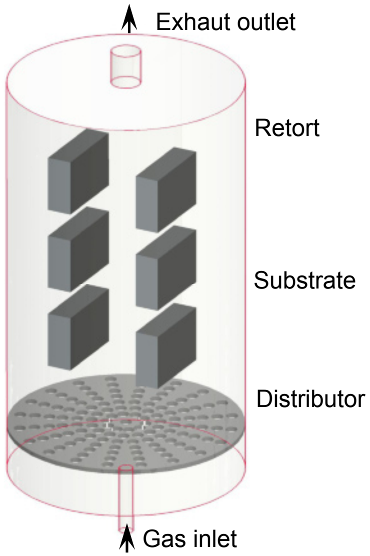

Figure 6.29. A typical solid model constructed using CSG method for a CVD system

It is also worth mentioning that 3-D objects can be simplified into 2-D structures. This simplification can reduce significantly the requirement for computational power hence much quicker for these problems.

6.4.3 Geometry Discretisation and Mesh Generation

Geometry using the above techniques is the first step. Trying to produce a single-solution method for any defined geometry and different types of flow is impractical, if not impossible, with current technology. The key with the numerical approach used in CFD is to divide the whole flow space or domain into many smaller and easy to understand subdomains (also called element or control volumes), which is known as the geometry discretisation and mesh generation process. The basis for this is that, though it is difficult to derive a single generic analytical solution to a complex problem, it is possible to develop solutions to smaller and well-understood elements within the fluid dynamic domain. For each of these well-understood types of elements, it is possible and relatively easier to derive a set of partial differential or integral-differential equations for the elements and use the required boundary conditions for each element to find solutions to the problem. During this process, it is reasonable and accurate enough to simplify the exact conservation laws for a given type of element. It is therefore often the case that a solution in the form of a particular set of equations is usually derived for a particular type of element. This approach hence ensures that the solution and computational efficiency can be optimised as general purpose tools, but they are usually not optimum for any one application.

The constituent subprocesses of discretisation consist of mesh generation (determining the types of mesh elements), space discretisation and time discretisation.

6.4.3.1 Mesh Generation Strategy

Once a solid object is modelled either in 2-D or 3-D, the next stage of the CFD working principles is to generate mesh elements for the volumetric space where a fluid flows. This effectively divides the whole volume space, often referred to as a domain, into a large number of so-called small elements which are more solvable. The volume space or domain is divided into fine, non-overlapping elements or cells, also called grids, which govern the accuracy of a CFD solution. Generally the finer the grids are, the better the solution accuracy. From a mathematical modelling point of view, this essentially transforms in most cases the partial differntial equations of a complex fluid system into a set of algebraic equations, which are much easier to solve.

The above process of generating elements and linking them through nodes is called discretisation or, more commonly, meshing. Unlike a structural FEA approach, CFD meshing deals with the flow space between geometric boundaries. The meshing process of a computer system effectively relies on the system to recognise the ‘space’, sometimes requiring the help of a user, to discretise them into many smaller elements which are determined by the definition of the element sizes. As a general guideline, the smaller the elements are, the larger the number of elements created for a system, and the longer it takes to solve a problem. From design feasibility study point of view, it is advisable that each design session start with a larger element size first in meshing and then go through the whole CFD process first so that a working solution is achieved before a refined solution can be generated. This approach can reduce the effort required to give a rough solution and avoid many scenarios where an inability to solve a particular problem is more likely to be caused by mistakes in the model and in boundary condition definitions, rather than in meshing.

For CFD discretisation, some methods are available in commercial systems. These common methods include finite difference (FD), finite volume (FV) and finite element (FE) methods. Each of them takes a different approach in approximating the differential equations essentially based on the Navie–Stokes equation. Their underlying approaches are similar and they all approximate differential equations by a system of algebraic equations for the variables in some set of discrete locations in space and time.

Depending on the methods used, there are potentially three types of meshes which can be generated during a meshing process, namely structured, block-structured and arbitrary or unstructured meshes. In a structured mesh, gridlines are used to represent the domain; these gridlines do not cross and only intersect with other family gridlines once, as shown in Figure 6.30a. Each mesh element is represented in Cartesian coordinates, as the mesh topology is equivalent to a Cartesian grid. A structured mesh is characterised by a mesh element arrangement where all interior nodes of the mesh have an equal number of adjacent elements. The most common meshes generated by a structured grid generator are typically

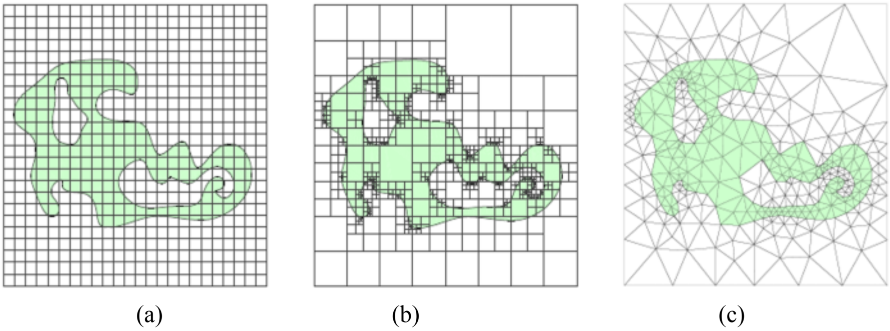
(a) (b) (c)

Figure 6.30. Examples of meshing methods: (a) structured, (b) block-structured and (c) unstructured

quadrilateral or hexahedral meshes. These mesh elements are only created for simple domains; other meshing techniques are required for more complex domains.

Block-structured meshes are an improvement over structured meshes as this approach allows the generation of a variable element number or element density in different blocks of the whole domain. Block structures are arranged in multiple levels based on the topology of the subdomain within the solution domain. On the top or coarse level of such a hierarchical strucutre, the whole domain is divided into blocks, which are a relatively large solution subspace of the domain. The structure of this subspace may not be regular and this subspace may or may not overlap with the block or subspace at a higher level of the hierachy. At the next low or fine level, a particular structure grid with a particular resolution is defined for each block. It is also necessary to undertake special treatments for block interfaces due to the above meshing difference. For some blocks, a lower level division is required to refine the mesh elements further to improve the accuracy of the CFD numerical analysis.

Unstructured meshes, as shown in Figure 6.30c, refer to the mesh elements generated by dividing an arbitrary solution domain boundary into a number of elements or control volume which may have any shape. There is no restriction on the element definitions. The most commonly generated element shapes are triangle or quadrilateral shapes in a 2-D domain, or tetrahedral or hexahedra shape in a 3-D domain. Unstructured mesh generation allows any number of elements to meet at a single node. This type of meshing increases the complexity of the data structures representing the meshes and can cause difficulties in computational implementation as the sparse matrix used in the analysis can require significant computer memory and may require the development of many special algorithms. On the other hand, due to their flexibility, these meshes are ideally suited for arbitrary domains and are amenable to adaptive mesh refinement.

6.4.3.2 Space Discretisation Method

With an accurate flow space or domain defined in terms of its geometry and a strategy for discretisaiton determined, it is necessary to select a suitable specific discretisation method before a problem can be solved. Having studied the field of fluid flow and dynamics for decades, researchers have developed a good set of mathematical solutions to different types of discretisstion problems. Each of these methods takes a different approach in approximating the differential equations essentially based on Navier–Stokes equations. All these discretisation methods approximate differential equations by a system of algebraic equations and only calculate the required variable values at these discrete locations in space and time. Due to the fact that these methods were developed for different problems, one method is therefore more suitable to the class of problems it was intended than others. In addition, the conservation equations can be written for different coordinate systems e.g. Cartesian, cylindrical, spherical, curvilinear orthogonal or non-orthogonal coordinate systems. For CFD space discretisation, there are a number of techniques and associated methods developed and available in commercial systems. The most important of these are finite difference (FD), finite volume (FV) and finite element (FE) methods as shown in Figure 6.31a–c respectively.

An FD-based method is a simple and straightforward method used and developed as a first approach to tackling the fluid flow problems using computers. The FD methods usually utilise Cartesian gridlines spaced out to represent the flow space, and the methods calculate the values of the relevant fluid dynamic parameters of interest for a number of gridline intersections points. In solving partial differentiation equations of a fluid system, this method essentially uses the linear combinations of the original function values at the gridline intersection points rather than their derivatives. This approximation enables the approach to simplify many complex partial differentiation calculations. Due to the simple gridline representations and the aforementioned approximation, their use is therefore largely restricted to the flow problems involving simple Cartesian geometries. FD has mostly been applied to structured or block-structured grids and meshes. FD methods utilise the differential form of the conservation equation.

In an FV method, the whole solution domain is subdivided into a finite number of contiguous control volumes. The computational node is located at the centroid of each control volume, whereas the node is located at the grid in the FD method. The FV method uses the integral form of the conservation equation

$$\int_S f dS = \sum_k \int_{S_k} f dS \tag{6.41}$$

This method is a widely adopted approach used most often in commercially available software systems. It is a method to represent, solve and evaluate partial differential equations as algebraic equations for the divided discrete volumes. In this approach, a small volume surrounding each node point on a mesh is defined and studied to calculate the relevant information such as the flow rate, temperature, etc. of this particular node using the ‘finite volume’. Applying the laws of conservation of mass, energy and momentum, the flux in terms of these three properties entering a given volume is always assumed to be identical to that leaving the adjacent volume. Based on this, starting from the volume element which is fully constrained and defined by the initial known boundary conditions,

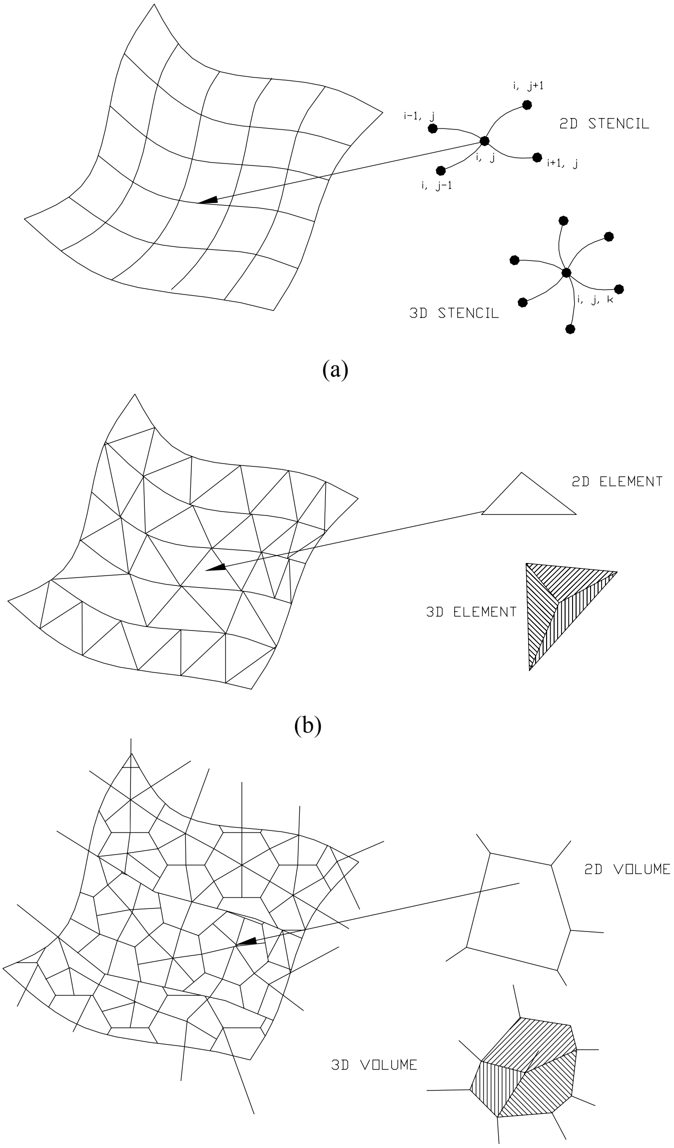

(a)

(b)

(c)

Figure 6.31. Examples of (a) FD, (b) FV and (c) FE meshing elements

the calculation of each element can be carried out and relevant information can be obtained.

The FE approaches used in CFD originate from structural mechanics and is similar to the FV method. A domain is divided into many discrete control volumes or finite elements. These elements are generally unstructured meshes. The most commonly used 2-D elements are triangles or quadrilaterals, whereas for 3-D meshing, tetrahedra or hexahedra are the most commonly generated meshes. In an FE method, weighting functions have to be selected, and this is the key distinguishing feature of an FE method compared with FV methods. For a given governing partial differential equation based on Navier–Stokes equations, it is possible to approximate it with a high-order polynomial equation. As this is an approximation, there is an error normally defined by a residual function. To accurately represent the original conservation law represented by a partial differentiation equation, an FE approach in CFD now involves to solving the problem of selecting the best solution with the minimum residual value, or ideally zero value for the residual.

6.4.3.3 Time Discretisation

Once a domain is discretised in terms of its space or geometry definitions for a given problem, it is also necessary to discretise the time – a process of determing the timing step value, as the computer based CFD analysis is essentially a discrete simulation technique. From conservation law equations, it is clear that all variables such as mass, momentum and energy vary in time, and the purpose of CFD analysis of a CVD process is to determine the performace of the system at any time. Depending on the problem, the time discretisation technique may vary. As the space and time variables are independent of each other, they can be discretised independently to obtain a sequence of normally non-linear algebraic systems.

For simple problems with simple geometries, the global time step for solving the conservation equations are normally set to be a constant step size determined by the stability constraint on the finest grid. The stability constraint referes to the step size at which the level of numerical errors, caused by the roundoff due to final precision of varible values represented in computers, should not be allowed to grow unboundedly.

For complex mesh types such as unstructred or block-structured meshes, it is necessary to adopt a ‘time-step-refined’ approach, where different suitablly defined time step sizes are employed for each mesh level [56]. Typically, this requires *recursive* integration on the various mesh levels, starting with the coarsest level (at a time step determined by the stability constraint of the mesh level itself), followed recursively by the integration of its child mesh levels, which are processed more often but at their (smaller) stability constrained time steps. Generally, this mulptilevel time stepping approach is commonly known as *subcycling*, which can be further improved by more rigorously defined methods using partitioned multirate time stepping [57], in which time step sizes are defined using more rational rules linking to the mesh types and mesh elements.

6.4.4 Boundary and Initial Conditions

For any given fluid dynamics problem, CFD-based simulation is normally used to evaluate the behaviour of a system for a limited domain or a bounded space. It is therefore important to define the fluid behaviour at the boundaries of this domain so the CFD analysis can be confined in a domain. Initial values of some flow properties should also be defined and can also be found from the understanding of the flow by investigating its initial definitions either when a steady state flow is fully developed or by giving dynamic values or a data table to define a function of the initial flow process.

6.4.4.1 Boundary Conditions

For CFD analysis of CVD systems, it is important to define correct boundary conditions for conservation equations. Typical example attributes of boundary conditions used in flow and heat transfer simulations are velocity, gas concentration, and temperature of the boundary areas. If an inlet boundary is selected such that it contains too many unknown initial values for the problem, one should extend the boundary area to as far as a bound where all initial variable values are known. In assigning the initial values of the boundary areas, it is a common practice to make the following assumptions [58, 59].

For solid walls, no-penetration and no-slip are typically applied to the momentum equation. Boundary conditions such as velocity, pressure and temperature at the inlet are usually known and specified, whereas their counterparts at the outlet are derived from assumptions of no-stress or fully developed and simulated flow. The thermal wall boundary conditions influence the flow significantly. Simple assumptions of constant wall temperature, insulated side walls and constant wall heat transfer flux have been used extensively for simple applications. More specifically, the following assumptions are normally made for a retort as shown in Figure 6.29 (the directions of the velocity in the following description refer to a cylindrical coordinate system in this figure).

On the walls, the normal and tangential velocities are assumed to be zero:

$$u_r = 0,\ u_\theta = 0,\ u_z = 0,\ T = const,\ P = const \tag{6.42}$$

At the inlet, the fluid has only an axial velocity according to either a parabolic or plug flow inlet profile:

$u_r = 0$, $u_\theta = 0$; $T = constant$, $P = constant$, $u_z = constant$ (for plug flow) or a predefined velocity profile,

$$u_z = 2u_0[1-(\frac{r}{R})^2],\ 0 \le \mathrm{r} \le \mathrm{R} \text{ for the parabolic inlet profile} \tag{6.43}$$

The outlet of the reaction chamber is assumed to be long enough that the velocity and temperature fields are fully developed:

$$\frac{\partial u_z}{\partial z} = 0, \frac{\partial u}{\partial z} = 0, \frac{\partial u_z}{\partial z} = 0, \frac{\partial T}{\partial z} = 0 \tag{6.44}$$

6.4.4.2 Initial Conditions

The initial flow attribute values are essential for the CFD solver to start the calculation with some known values in order to derive the fully understood element by working out all required flow property parameter values. For a CVD system, these initial values include the gas inlet speed, temperature and pressure and the temperature of the chamber wall and the substrates. The inlet initial gas flow properties are given as:

$$T = T_{0,}\ P = P_{0,}\ u = u_0 \tag{6.45}$$

As a first approach, the wall and substrate temperatures are assumed to be given. The initial conditions of the chamber wall and the substrates are also assumed to be given:

$$T = T_w\ (on\ the\ wall),\ T = T_s\ (on\ the\ substrate) \tag{6.46}$$

In addition, the variable values for physically non-negative attributes such as density must always be positive or meaningful for other values to be in a sensible range, e.g. concentration between 0 and 100 %.

6.4.5 Iterative Problem Solving Strategy

Depending on the space discretisation techniques used, the set of equations to be solved may be different, but for FD- and FV- based methods, the discretisation results in a set of linear or non-linear algebraic equations. These depend on the nature of these partial differential equations and how they are derived. For linear equations, it is well known that a Gauss elimination method can be used as a basic method to solve them. Further details of the Gauss method can be found in [60].

The Gauss elimination method can equally be used to solve any set of algebraic equations. However, this method is often expensive to use as there are still a large number of elements in the triangular matrices to use a direct method to solve them. Furthermore, the algebraic systems to be solved are very large and may contain millions of unknowns. For many such problems, these matrices are sparse, and most of the matrix coefficients are equal to zero. Gauss elimination methods are not effective for these problems. This brings about the necessity of employing iterative methods even sometimes for linear problems.

For non-linear algebraic equations and sometimes for linear problems as discussed above, an iterative method must be used, in which an initial solution is estimated or guessed and it in turn is used in the equations to systematically improve its accuracy. Non-linear problem solving techniques can be classified into two broad groups: Newton-like methods and global solving methods. Newton-like methods are effective and efficient in solving non-linear problems provided the initial estimated solution is available and closer to the final solution. Otherwise, they may fail to solve the problem completely. Global methods, on the other hand, can guarantee to derive an existing solution by searching all solution spaces. It is therefore not an efficient and fast approach to finding solutions. Whichever methods are used, this iteration process continues until, under an ideal situation in most cases, the solution gradually approaches the target solution, in which case the solution converges.

Assume that a solution after the *n*th iteration is represented as Φ_n which contains a set of values of interest (e.g. temperature, velocity, etc.) for all elements of a domain. The converged solution can be represented by Φ, and the residual after the *n*th interaction can be expressed as:

$$\epsilon_n = \Phi - \Phi_n \tag{6.47}$$

The purpose of interactive calculation is to drive the residual error ϵ_n to zero. The process of deriving a solution Φ_n which is close to the problem solution is called a converging process. In a typical interactive problem solving process, there are two levels of iteration, namely outer iterations and inner iterations. During outer iterations, the coefficients of the discrete problems are recalculated and updated for more accurate representations of these coefficients, using the solution values of the fluid flow system from the previous iteration. During these calculations, Newton-like methods are used to eliminate the non-linearities of the fluid problem such as those defined in previous sections. Coupled equations are also segregated so that these governing equations of the fluid system can be solved. For the inner iterations, linear equations or subproblems are solved by an iterative method, such as conjugate gradients introduced by Golub and van Loan [61], biconjugate gradients proposed by Fletcher, or a strategy-based multigrid approach [60]. If direct solvers such as Gaussian elimination are to be used, they require large and expensive computer resources both in terms of memory required and time taken. It is therefore common to use iterative approaches to solve these problems.

During the course of interactive problem solving, it is important to know when to stop the iteration if the solution converges. This has a great impact on the solution accuracy as well as problem solving efficiency. The ultimate factor determining this is the errors produced at the end of each iteration during the problem solving. If these errors reach an acceptable level, the numerical problem solving can be stopped. Otherwise the iterative problem solving carries on until an acceptable solution is found, or unless the problem solution is not converging. The solution errors come from each part of the process used to produce numerical solutions, as detailed in the following sources: (1) modelling errors: these define the difference between the actual flow and the exact solution of the mathematical model; these errors include geometrical representational errors from geometric models of a physical fluid flow system; (2) discretisation errors: these are defined as the difference between the exact solution derived from the equations of the laws of conservation of mass, momentum and energy and the converged solution of the discretised system; and (3) iteration errors; these are the difference between the exact solution of the algebraic equation systems and that from a solution after so many iterations.

Using the above errors in a CFD interative problem solving process, it is necessary and possible to check the residuals, relative solution changes and other indicators to make sure that the solutions converge after certain iterations. Computer algorithms have been implemented based on these indicators to stop the calculations once a certain level of errors is reached based on the calculations of the above three types of residual errors. Using a CFD software system in this process is relatively easy and simple and all that is normally required is patience to see the results. Depending on the compexity of the problem, solving can take hours if not days before it finishes. In some cases, the results of the problem solving may not produce the expected results due to a number of reasons, including wrong initial or boundary conditions defined, meshes are too coarse, or elements are too small for the computer to solve. It is important to read the error message from the software system to rectify any problems in the model or initial specifications.

6.4.6 Postprocessing and Visualisation

The main function of postprocessing and visualisation in CFD is to process the simulation results derived from the computed flow field and externalise them in a suitable and comprehensible format. Any deficiency identified at this stage can be eliminated without incurring any costs associated with physically building these systems. More specifically, postprocessing deals with the calculation of derived parameter quantities for velocity and stream function in a fluid flow system. These can help CVD system designers and process engineers to identify suitable process control parameters such as drag, total mass and lift to ensure constant flow velocity can be established by adjusting inlet initial reactant gas control parameters, such as pressure, temperature, etc. For delicate coating applications, a slight mismatch of gas velocity to the required one may cause the whole process to be substandard and the products coated may not achieve the expected behaviour.

Visualisation is a process of converting all data for one parameter or a set of parameters of interest into a more visual graphical representation to help users of the CFD systems to quickly visualise the results. The format of this visual externalisation of the results can be in one dimension, showing a number of values of a particular system performance parameter in a series of line segments in a chosen colour and line types (solid line, dashed lines, dotted line, etc.). In a 2-D representation of function values, two sets of data are used to form a 2-D curve, which could represent streamlines of a flow, isobaric contours showing the areas where the pressures are the same. Alternatively, colour diagrams are used to indicate the different levels of functional parameter values using different colours which normally have an indicative value besides the colour diagrams.

For 3-D representations, similar functional parameter values can be shown for a 3-D feature, such as surfaces, volumes and cut planes. To represent the magnitude of the functional parameter values, arrows can also be used to give a less scattered representation. Arrow plots are usually used to represent the flow directions and vortexes formed and they are particularly suitable for representing flow directions within the solution domain as these arrows can give clear directional information.

6.4.7 Some Computational fluid dynamics Application Examples

6.4.7.1 Influence of the Number and Arrangements of Components on the Flow Field

A CFD technique can be used to evaluate the behaviour of a CVD system. Here some examples are given to show its applciaitons and effectiveness to understand how systems work and how to design a process for a system. Figure 6.32 shows the simulation results of flow patterns and gas distribution inside a reaction chamber

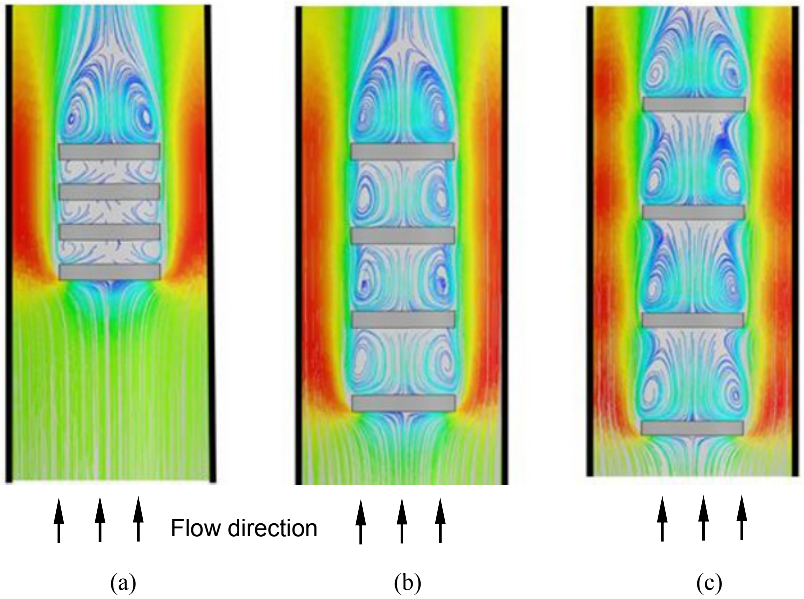

Figure 6.32. Flow velocity profile of stream lines around the components horizontally arranged in the reaction chamber: (a) 50 mm, (b) 100 mm and (c) 150 mm

where the components are arranged in 4 × 1 (four components arranged vertically in one column). The components to be deposited are arranged horizontally and the distance between the components is changed from 50 mm to 100 mm and then 150 mm. Assume that the plug gas flow is introduced into the reaction chamber from the bottom. The flow approaches the first component at the bottom of the chamber and is diverted horizontally and then squeezed into the gaps between the components and chamber wall. The flow velocity along this circumferential ring, which is also called a main stream flow, is much faster than that in the other areas as indicated by the densities of the stream lines. Between the components, the gas flow is very slow and there are some recirculations as shown in Figure 6.32.

When the reactant precursor gases flow passing the sides of the components, their velocities increase as they pass through a narrow gap. After passing through the narrowest area, they form vortexes or recirculations as the velocity decreases. When the distance is 50 mm, there is a stagnant flow area between the components, as shown in Figure 6.32a. When the distance between components is increased to 100 mm and 150 mm as in Figure 6.32b and c, there are recirculations between the components. The recirculation leads to the longer residence time of the gases between the components. This in turn results in poor deposition quality because the exhaust gases cannot be removed in time and the reactant gases cannot be delivered onto the surface of the substrate. Meanwhile, the quality of the deposition on the central area of a component varies significantly on the sides of the component as they experience different flow velocities of the reactant precursor gases. It is clear that the arrangements and the number of components in a reaction

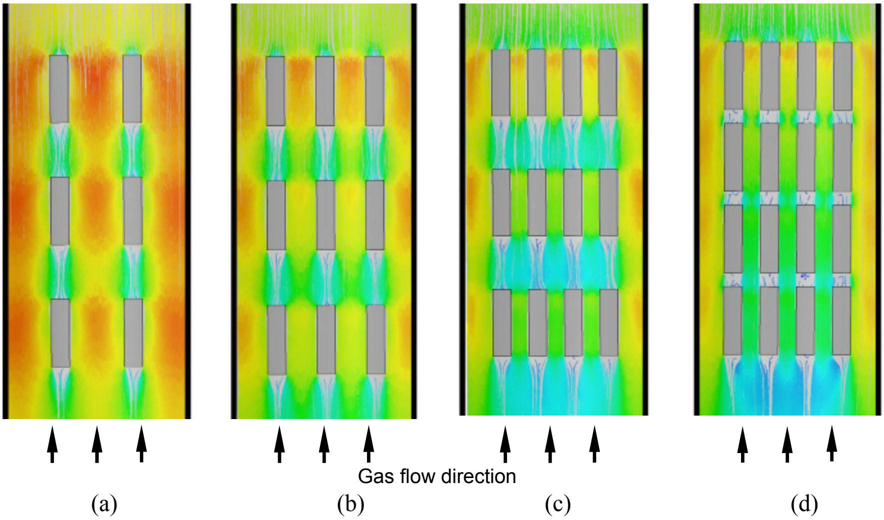

Figure 6.33. Flow velocity profile around the components vertically arranged in the reaction chamber: (a) 2 × 3, (b) 3 × 3, (c) 4 × 3 and (d) 4 × 4

chamber has a significant impact on the gas flow patterns and the deposition quality.

As shown in Figure 6.33, the components are arranged in 3 × 2 (three components arranged vertically in two columns), 3 × 3, 4 × 3 and 4 × 4 layouts. When the components are arranged vertically, the flow becomes much less restrictive and several main stream flows can be formed depending on the number of columns of the components. The number of components in each row also determines the flow pattern and the smoothness of the main stream flows. Figure 6.33 shows four different arrangements of components and their gas flow simulation results. As the number of columns increases, the gas flow becomes smoother and the quality of gas flow also improves with more constant flow speed. This can be explained by the decreases in free volume within the reaction chamber according to Equation (6.23). As the free volume decreases, the residence time becomes shorter, hence leading to the better deposition quality. In addition, the free convection of the gas flow can also be eliminated as the characteristic distance decreases according to Equation (2.64).

From the simulation results it can also be seen that residence time is not only dependent on the free volume but also on the arrangements of the components within a reaction chamber. This observation through simulation results is not reflected in Equation (6.23).

6.4.7.2 Optimisation Design of Flow Profile for Components with Complex Shape

For simple components such as plates and flat disks, the above simple change of arrangements is effective and can be optimised to ensure an approximately constant flow velocity, which in turn ensures uniform deposition. For components with complex shapes, such as domed components as shown in Figure 6.34, it is

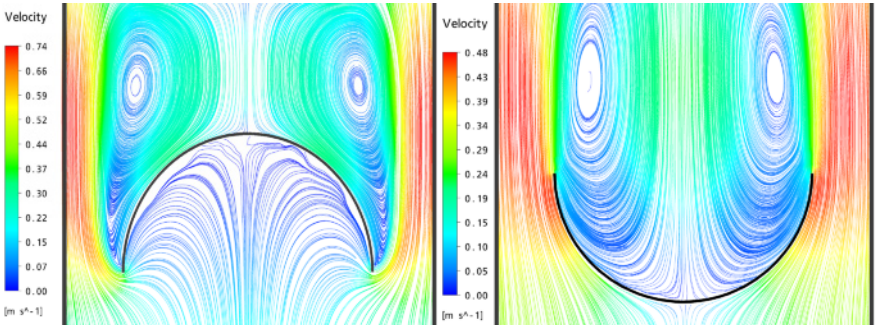

(a) (b)

Figure 6.34. Flow profile around dome-shaped component: (a) Facing downstream and (b) Facing upstream

important to study the arrangement of such components inside the chamber. In many cases, there exist stagnant gas flow behaviours in some parts of the component and it is therefore necessary to design a gas flow guidance device to ensure a relatively smooth and constant precursor gas flow passing through the components. This approach depends on the shape of the components and has to be dealt with in a case-by-case manner. Simulation based on CFD can faciliate a rapid evaluation of gas flow velocity of such components in a predefined chamber and help designers and manufacturers to decide how they can produce high-quality CVD components. The following section shows a CFD simulation analysis and the design of a sample product.

Taking a domed component as an example, the precursor gases inside the

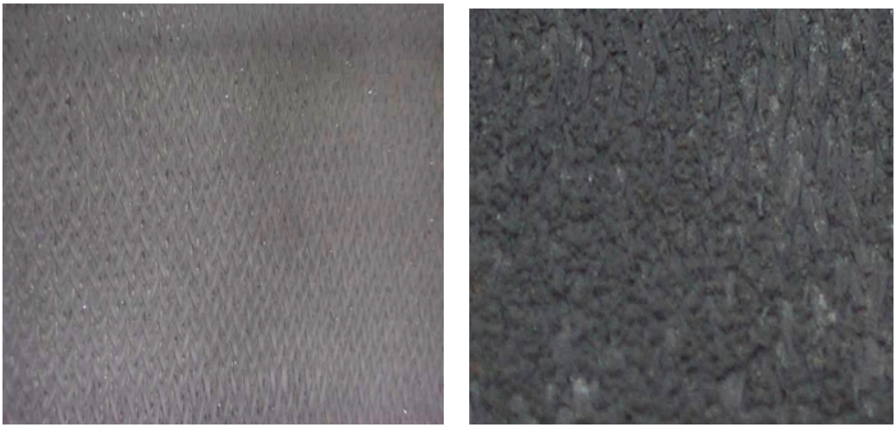

(a) (b)

Figure 6.35. Deposition quality comparison of both sides of a dome-shaped component corresponding to the arrangement of Figure 6.34b: (a) Smooth outside of the component (b) Coarse inside

component tend to be trapped if the component is placed as shown in Figure 6.34a. Near the centre of the dome underside is a stagnant gas flow area and the velocity near the circumference of the upper side is also very slow. These two types of gas flows on the same component can lead to poor and uneven deposition on the surface of the component. When the component is arranged upside down as shown in Figure 6.34b, there is a more consistent gas velocity near the underside of the component. On the upper side, there are severe recirculations. These contrasting flows on both sides of the component result in clearly different qualities of deposition. As the underside of the component experiences more consistent precursor gas flow, the deposition quality is much better than that at the top side of the component.

Figure 6.35 shows the deposition quality on both sides of a domed component when it is placed in Figure 6.34b for deposition. The component is a fibre preform prepared by the 3-D braiding method. The outside of the component is smooth whereas the inside is very coarse.

It is clear that it is impossible to solve the poor deposition quality problem by simply arranging the orientation of the complex shaped components. Based on the above simulation results and applying the principle of minimising the residence time inside the reaction chamber, techniques on the process design and associated tools have been developed to solve the above problems. Central to these techniques is the introduction of a gas flow guidance tool according to the geometric shape of the complex components. These guidance tools are designed to force and optimise the gas flow consistently around the component to be deposited. Such a design of a gas flow guidance tool for the domed component is as shown in Figure 6.36. The reactant precursor gases can only flow following the directions indicated by the arrows as no other flow path is allowed.

Once again, a CFD-based simulation tool can be used to evaluate the effect of such a design. Figure 6.37 shows the simulation results and effects of three such gas flow guidance tools, where the distance between the component deposition surface and the guidance tool inner surface is about 30 mm and the opening angle of the guidance tool varies from 30°, 60° and 90°. The precursor gases are introduced into the centre of the domed part of the component where they are

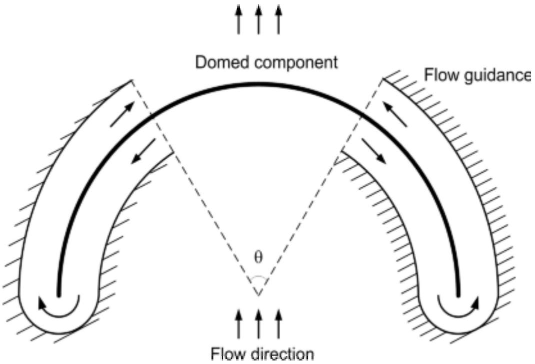

Figure 6.36. Schematic diagram of a domed component with flow guidance tool

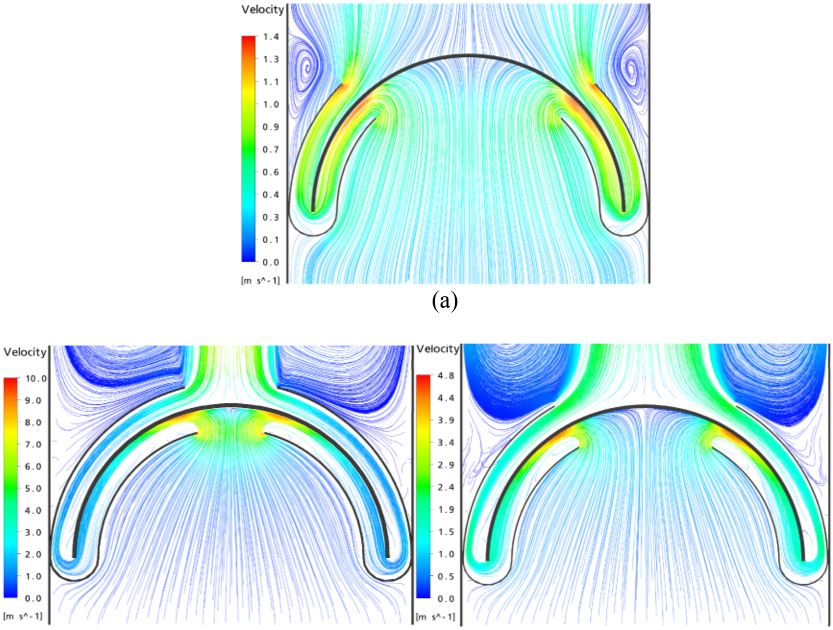

(a)

(b) (c)

Figure 6.37. Velocity profile of stream lines by complex guidance tool with a distance of 30 mm between the component and the tool: (a) $\theta = 90°$, (b) $\theta = 60°$ and (c) $\theta = 30°$

forced to flow downwards inside the channel between the component and the flow guidance. Then, the gases change direction after they reach the bottom edge of the component, thereafter upwards along the component surface.

By introducing such a flow guidance tool, it is clear from the simulation results that there is neither a stagnant gas flow area nor recirculations in any part of the component surface. This effectively solves the problems encounted in the arrangements shown in Figure 6.34a and b. Therefore, uniform deposition on both sides of the component can be ensured and the deposition quality can be significantly improved.

Figure 6.37 shows the comparative evaluation and some simulation results of three scenarios when the θ angle as defined in Figure 6.36 is 90° (a), 60° (b) and 30° (c). When θ is 90°, the component experiences much slower average gas velocity ranging from 0 to 1.4 $\mathrm{m \cdot s^{-1}}$. When θ is decreased to 60°, the average velocity is increased, as does the velocity range across the component surface. When θ is further reduced to 30°, the velocity over the whole component surface increases significantly to a range of 1.5 to 8 $\mathrm{m \cdot s^{-1}}$. The stagnant flow area has also been reduced compared with the other two scenarios. These results clearly show the difference in velocity and its profile without the need for experiments. The actual effects of the gas guidance tool on the deposition quality require further experimental confirmation.

References

[1] Vignoles G, Goyheneche J, Sebastian P, Puiggali JR, Lines JF, Lachaud J, Delhaesc P, Trinquecostec M (2006) The film-boiling densification process for C/C composite fabrication: from local scale to overall optimization. Chem Eng Sci 61:5636–5653

[2] Spear KE, Dirkx RR (1990) Predicting the chemistry in CVD system. In: Besmann T M, Gallois B M (eds) Chemical vapour deposition of refractory metals and ceramics. Materials Research Society, Pittsburgh, PA, pp19–30

[3] Kaiser N (2002) Review of the fundamentals of thin-film growth. Appl Opt 41:3053–3060

[4] Petrov I, Barna PB, Hultman L, Greene JE (2003) Microstructural elvolution during film growth. J Vac Sci Tech A21:S117–S128

[5] Winand R (1994) Electrodeposition of metals and alloys-new results and perspectives. Electrochim Acta 39:1091–1105

[6] Landolt D (2002) Electrodeposition science and technology in the last quarter of the twentieth century. J Electrochem Soc 149:S9–S20

[7] Bauer E (1958) Phanomenologische theorie der kristallabecheidung an oberflachen, I-II. Z Kristallogr 110:372–394

[8] Bloem J (1980) Review: nucleation and growth of silicon by CVD. J Cryst Growth 50:581–604

[9] Movchan BA, Demchishin AV (1969) Investigations of the structure and properties of thick Ni, Ti, W, Al_2O_3 and ZrO_2 vacuum condensates. Phys Met Metallogr (USSR) 28:83–90

[10] Thornton JA (1977) High rate thick film growth. Annu Rev Mater Sci 7:239–260

[11] Thornton JA (1974) Influence of apparatus geometry and deposition conditions on the structure and topography of thick sputtered coatings. J Vac Sci Technol 11:666–669

[12] Hwang NM, Yoon DY (1994) Driving force for deposition in the chemical vapour deposition process. J Mater Sci Lett 13:1437–1439

[13] Lespoaux D, Langlais F, Naslain R (1995) Correlations between gas phase supersaturation, nucleation process and physico-chemical characteristics of silicon carbide deposited from Si-C-H-Cl system on silica substrate. J Mater Sci 30:1500–1510

[14] Bryant WA (1977) Review: the fundamentals of chemical vapour deposition. J Mater Sci 12:1285–1306

[15] Blocher JM (1974) Structure/property/process relationships in chemical vapour deposition CVD. J Vac Sci Technol 11:680–686

[16] Nakashima S, Matsunami H (eds) (1995) Silicon carbide and related materials. Institute of Physics, Bristol, UK

[17] Wagner RS, Ellis WC (1964) Vapor-liquid-solid mechanism of single crystal growth. Appl Phys Lett 4:89–90

[18] Pan ZW, Xie SS, Chang BH *et al.* (1999) Direct growth of aligned open carbon nanotubes by chemical vapour deposition. Chem Phys Lett 299:97–102

[19] Motojima S, Ueno S, Hattori T, Goto K (1989) Growth of regularly coiled spring-like fibers of Si_3N_4 by iron impurity-activated chemical vapor deposition. Appl Phys Lett 54:1001–1003

[20] Callister W d Jr (2007) Materials science and engineering: an introduction, 7th edn. Wiley, New York

[21] Spencer MG ed, (1994) Silicon carbide and related materials. Institute of Physics, Bristol, UK

[22] Nakashima S, Matsunami H (eds) (1995) Silicon carbide and related materials. Institute of Physics, Bristol, UK

[23] Vahlas C, Caussat BG, Serp P (2006) Principles and applications of CVD powder technology. Mater Sci Eng R53:1–72

[24] Xu YD, Cheng LF, Zhang LT, Zhou WC (1999) Morphology and growth mechanism of silicon carbide chemical vapor deposited at low temperature and normal atmosphere. J Mater Sci 34:551–55

[25] Niihara K, Hirai T (1976) Chemical vapour-deposited silicon nitride: Part 1: Preparation and some properties. J Mater Sci 11:593–603

[26] Nicolis G, Prigogine I (1977) Self-organization in non-equilibrium systems. Wiley, New York

[27] Messier R, Yehoda J E (1985) Geometry of thin-film morphology. J Appl Phys 58:3739–3746

[28] Coffin LF (1964) Structure-property relations for pyrolytic graphite. J Am Ceram Soc 47:473–478

[29] Komiyama H, Shimogaki Y, Egashira Y (1999) Chemical reaction engineering in the design of CVD reactors. Chem Eng Sci 54:1941–1957

[30] Saito T, Shimogaki Y, Egashira Y *et al.* (1992) Conformal deposition of WSi_x films on micron-sized trenches: the reactivity of film precursors. Appl Phys Lett 61:764–765

[31] Saito T, Oshima K, Shimogaki Y, Egashira Y, Komiyama H (1993) A kinetic study of CVD-WSi_x processes–the comparison of WF_6/SiH_4 and WF_6/Si_2H_6 processes. In: Jensen K N, Cullen G W (eds) Proceedings of the 12th international conference on chemical vapour deposition. Honolulu, HI, Electrochemical Society. Pennington, NJ, pp238–243

[32] Saito T, Shimogaki Y, Oshima K, Egashira Y, Sugawara K, Takahiro K, Nagata S, Yamaguchi S, Komiyama H (1994) Gas phase chemistry determining silicon contents in CVD WSix process. Materials Research Society Conference Proceedings 9. Advanced Metallization for ULSI Applications in 1994, pp475–479

[33] Hong LS, Komiyama H (1991) Chemical vapor deposition of CuO_x films by CuI and O_2: role of cluster formation on film morphology. J Am Ceram Soc 74:1597–1604

[34] Huttinger KJ (1998) CVD in hot wall reactions-the interaction between homogeneous gas-phase and heterogeneous surface reactions. Chemical Vapor Deposition 4:151–158

[35] Huttinger KJ (2003) Fundamentals of chemical vapour deposition in hot wall reactors. In: P Delhaes (ed) Fibres and Composites. Taylor & Francis, London, pp75–86

[36] Benzinger W, Becker A, Huttinger KJ (1996) Chemistry and kinetics of chemical vapour deposition of pyrocarbon: I. Fundamentals of kinetics and chemical reaction engineering. Carbon 34: 957–966

[37] Ferona O, Langlaisa F, Naslaina R, Thebaultb J (1999) On kinetic and microstructural transitions in the CVD of pyrocarbon from propane. Carbon 37: 1343–1353

[38] Hu ZJ, Zhang WG, Huttinger KJ, Reznik B, Gerthsen D (2003) Influence of pressure, temperature and surface area/volume ratio on the texture of pyrolytic carbon deposited from methane. Carbon 41:749–758

[39] Thomas J M, Thomas W J (1997) Principles and practice of heterogeneous catalysis. VCH, Weinheim

[40] Adamson AW, Gast AP (1997) Physical chemistry of surfaces. Wiley, New York

[41] Lieberman ML, Pierson HO (1974) Effect of gas phase conditions on resultant matrix pyrocarbons in carbon/carbon composites. Carbon 23:233–241

[42] Delhaes P (2002) Chemical vapour deposition and infiltration processes of carbon materials. Carbon 40:641–657

[43] Watanabe K, Komiyama H (1990) Micro/macrocavity method applied to the study of the step coverage formation mechanism of SiO_2 films by LPCVD. J Electrochem Soc 137:1222–1227

[44] Dutta S, Rice RW, Graham HC, Mendiratta MC (1980) Characterization and properties of controlled nucleation thermochemical deposition (CNTD)-silicon carbide. J Mater Sci 15:2183–2191

[45] Holzl RA (1980) Deposition method and products. US Patent 4,239,819

[46] Bryant WA (1976) Producing extended area deposits of uniform thickness by a new chemical vapour deposition technique. J Cryst Growth 35:257–261

[47] Delhaes P (2002) Review: chemical vapor deposition and infiltration processes of carbon materials. Carbon 40:641–657

[48] Douglas JF, Gasiorek JM, Swasffield JA, Jack LB (2005) Fluid mechanics, 5th edn. Pearson, London

[49] Munson BR, Young DF, Okiishi TH (2006) Fundamentals of fluid mechanics, 5th edn. Wiley, New York

[50] Mironer A (1979) Engineering fluid mechanics. McGraw–Hill, New York, pp287–288

[51] Ferziger JH, Peric M (2002) Computational methods for fluid dynamics, 3rd edn. Springer, Berlin Heidelberg New York

[52] Anderson JD Jr (1995) Computational fluid dynamics: the basics with applications. McGraw–Hill, New York

[53] Bird RB, Stewart WE, Lightfoot EN (1960) Transport phenomena. Wiley, New York

[54] Incropera FP, Dewitt DP, Bergman TL, Lavine AS (2007) Fundamentals of heat and mass transfer, 6th edn. Wiley, New York

[55] Thomson WJ (2000) Introduction to transport phenomena. Prentice Hall, Engelwood Cliffs, NJ

[56] Berger M, Oliger J (1984) Adaptive mesh refinement for hyperbolic partial differential equations. J Comput Phys 53:484–512

[57] Gunther M, Kværno A, Rentrop P (2001) Multirate partitioned Runge–Kutta methods. BIT 41:504–514

[58] Jensen KF (1993) Fundamentals of chemical vapour deposition. In: Hitchamn ML, Jensen KF (eds) Chemical vapour deposition: principles and applications. Academic, San Diego, CA, pp31–90

[59] Fotiadis DI, Kieda S (1990) Transport phenomena in vertical reactors for metalorganic vapour phase epitaxy. J Cryst Growth 102:411–470

[60] Fletcher R (1976) Conjugate gradient methods for indefinite systems. Lecture Notres in Mathematics, vol 506. Springer, Berlin Heidelberg New York

[61] Golub GH, Van Loan C (1990) Matrix computations. Johns Hopkins University Press, Baltimore, MD